12-2013

Modeling and Validation of Heat Transfer Present in a Solar Thermal Collector

Eric Ezekiel Stannard
University of Tennessee - Knoxville, estannar@utk.edu

To the Graduate Council:

I am submitting herewith a thesis written by Eric Ezekiel Stannard entitled "Modeling and Validation of Heat Transfer Present in a Solar Thermal Collector." I have examined the final electronic copy of this thesis for form and content and recommend that it be accepted in partial fulfillment of the requirements for the degree of Master of Science, with a major in Mechanical Engineering.

William A. Miller, Major Professor

We have read this thesis and recommend its acceptance:

Tricia A. Stuth, Rao V. Arimilli

Accepted for the Council:
Carolyn R. Hodges

Vice Provost and Dean of the Graduate School

(Original signatures are on file with official student records.)

Modeling and Validation of Heat Transfer Present in a Solar Thermal Collector

A Thesis Presented for the

Master of Science

Degree

The University of Tennessee, Knoxville

Eric Ezekiel Stannard

December 2013

Acknowledgments

This work would not have been possible without the guidance and support of my advisor, Dr. William Miller. I would also like to thank Tricia Stuth of the College of Architecture and Design for the funding of this work and the sharing of field data from the New Norris House. Thank you to Samuel Mortimer and Tony Gehl for always being there to answer my technical questions. And thank you and apologies to Valerie Friedmann for enduring my repairs.

Lastly, thanks to my close friends, John and Emily Clark, Jordan Sawyer, and Michael Merriweather for making my time at UT an enjoyable one.

Abstract

A solar absorber panel for a solar water heating system located at the College of Architecture's New Norris House in Norris, TN was modeled and validated against field data in this work. The purpose of this modeling was to create the foundations of a tool that can be used in collector design and building energy simulations. This tool would take into account the radiometric properties of the collector materials, which are essential for an accurate model. Solar water heaters convert the shortwave energy of the Sun into usable heat for residential and industrial applications and have the potential to greatly reduce building energy consumption. Using measured field site data including global solar irradiance, outdoor air temperature, and incoming working fluid temperature, a heat transfer model was created in FORTRAN 95 to predict the energy that the installed collector could deliver to the working fluid. Shortwave radiation and its interaction with glass were also considered. First principles were used to create a system of equations to predict the glass, absorber, and fluid temperatures. Computed capacity and heat gains and losses were used to estimate system efficiency and efficacy. The predicted working fluid temperatures were compared against the field site data for validation. For the days chosen for validation, the model predicted the working fluid temperature at the heat exchanger with an average absolute error of 0.6 °[degrees] C. The model was also benchmarked against two laboratory conditions provided by the collector's manufacturer, with errors of 0.5 and 0.1 °[degrees] C. Several design aspects of the solar absorber panel were unknown, and a sensitivity analysis was performed to demonstrate unknown parameters' effects on predicted temperature. Wind speed had a negligible effect at low velocities but became noticeable at speeds that caused turbulent flow on the top plate. The unknown glass reflectance had an insignificant effect.

Table of Contents

List of Tables

List of Figures

Nomenclature

A	area
$Ab_{a,b}$	absorbtance of layer a, surface b
c_p	specific heat
D	diameter
$\dot{E}$	energy rate
f	friction factor
F	view factor
g	gravitational acceleration
h	local heat transfer coefficient
$\bar{h}$	average heat transfer coefficient
$\check{h}$	combined heat transfer coefficient
H_{az}	height of cavity space between bottom of collector and roof
H_g	height of internal collector cavity between glass and absorber
I	normal component of global irradiance
k	thermal conductivity
L	thickness
$\dot{m}$	mass flow rate
Nu	local Nusselt number
$\overline{Nu}$	average Nusselt number
Pr	Prandtl number
$q_{i\ a,b}$	shortwave radiation into layer a, surface b
q''_{loss}	heat flux leaving bottom of collector
q'''	thermal generation
R	resistance to heat transfer
Ra	Rayleigh number
Re	Reynolds number
$Rf_{a,b}$	reflectance of glazing layer a, surface b
T	temperature

Tr_a	transmittance of layer a
W	longer dimension of the collector
x^+	dimensionless distance
x	distance into pipe
y	depth into glass pane

ε	emissivity
η	collector efficiency
ρ	density
σ	Stefan-Boltzmann constant
τ	tilt angle
τ^*	critical tilt angle
μ	dynamic viscosity
ω	relaxation factor

Chapter 1: Introduction

Solar water heaters (SWH) have been commercially available since 1891[1]. Unlike photovoltaic technology which produces electricity from sunlight, they convert the Sun's energy directly into thermal energy for water heating use. Earth's solar constant is 1.37 kW/m^2 at the outer atmosphere[2], making solar energy readily available. Using the sun to heat water for residential use makes practical sense. In modern SWHs an absorber panel is mounted exterior to a home. It is designed to absorb the shortwave radiation of the Sun and convert it to usable heat[2]. As the only electrical requirement for SWHs is a relatively small pump for the transferring fluid between the collector and storage tank and its electronic controller, it has the potential to deliver large amounts of energy to the water at little operating cost.

Figure 1 shows a breakdown of where energy is used in U.S. homes furnished by the Energy Information Administration[3]. As of 2009, water heating accounted for 17.7% of home energy use, consuming 1.8 quadrillion BTUs ($5.28*10^{11}$ kWh) of energy for the year. Implementing SWHs in 50% of U.S. homes could save upwards of 1 Quad of energy. Clearly a reduction in energy use for water heating would lead to significant reduction in national energy consumption.

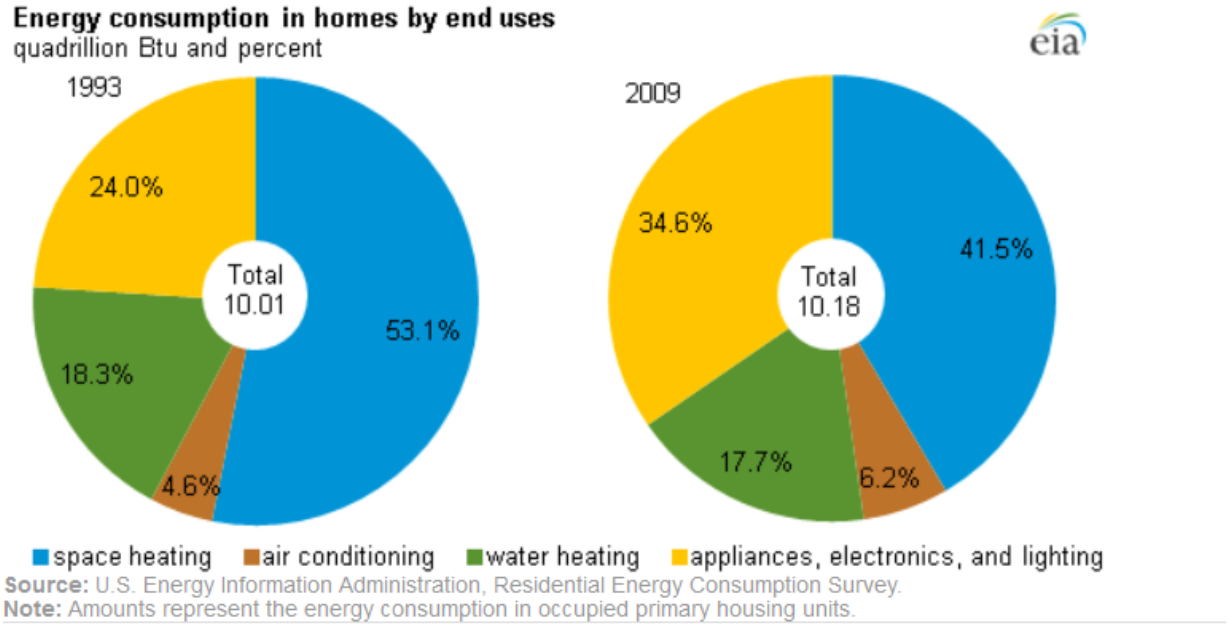

Figure 1. Breakdown of U.S. Home Energy Use[3]

In this work, a model which predicts fluid and absorber component layer temperatures will be developed using heat transfer first principals. This model will serve as the groundwork for a code that incorporates the radiometric properties of glazings for use in the design of cold climate solar thermal collectors. The model will be validated against a single pane flat plate solar collector located at the University of Tennessee College of Architecture's New Norris House.

There are two types of solar water heater configurations. A direct system pumps the water that is to be heated directly through the absorber panel[2]. Piping inside the solar collector becomes heated by the Sun, transferring energy to the water inside it. The pipe then extends from the panel to the water storage tank, supplying it with hot water. Since the water loop is partially external to the home, it is susceptible to freezing. Because of this, a direct system should only be employed in regions where freezing is not a concern.

The other type of system is an indirect system, which is the type of system under study at the New Norris House. A fluid is pumped through the absorber panel to collect heat which transfers its energy to a plate heat exchanger external to a standard water storage tank[2]. Water from the storage tank is thermally syphoned through the heat exchanger to absorb the heat. To prevent pipe bursts from freezing and expansion, an

antifreeze solution referred to as the working fluid is used as the fluid that passes through the solar collector. Figure 2 shows an example of a solar collector panel's cross section.

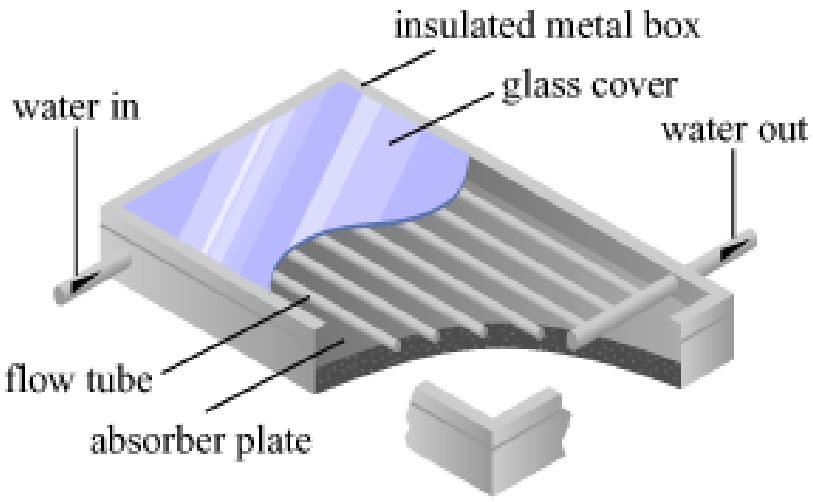

Figure 2. Solar Thermal Collector Cross Section[4]

Hudon et al.[5] recently created a report detailing markets and technological barriers for the implementation of SWH technology. Figure 3 shows their predicted savings of two water heating technologies, heat pump water heaters (HPWHs) and SWHs, as compared to natural gas water heaters in cities within three different climate zones. In three of those cities, converting from a natural gas water heater to a HPWH actually results in a net increase in energy use. The HPWH absorbs heat from the inside of the home, which causes additional heating loads, especially in colder climates. Conversely, solar water heaters show a savings in energy use regardless of location.

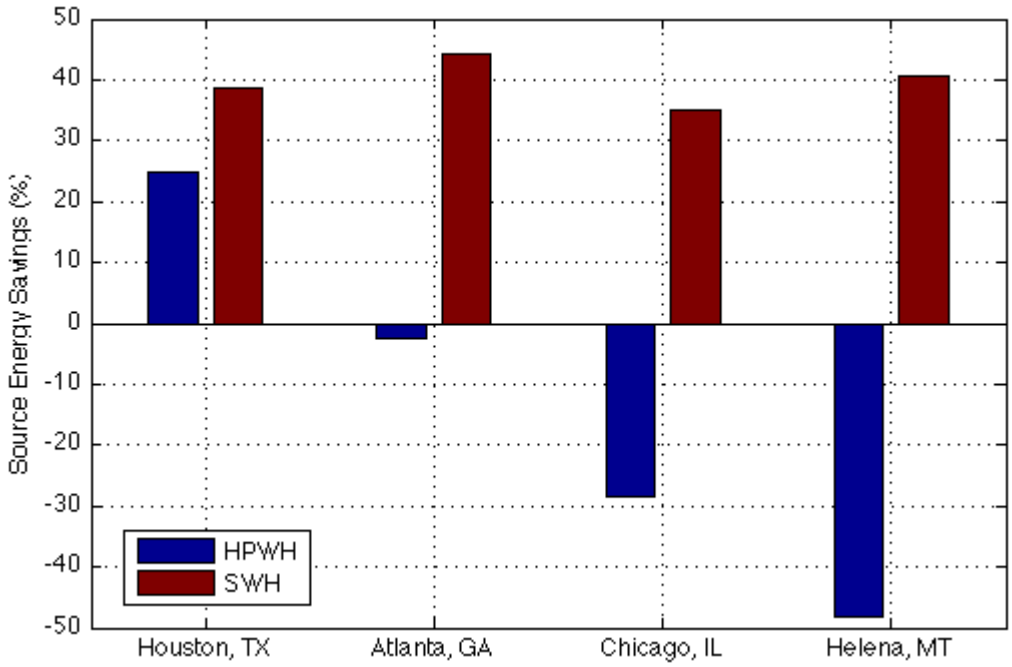

Figure 3. Energy Savings of HPWH and SWH Technologies Relative to Gas WH[5]

Their work also shows a map of the United States with select cities marked as "Go" or "No Go." The red "Go" cities represent locations where replacing gas water heaters with HPWHs results in source energy savings, while the blue "No Go" cities signify locations where more source energy would be used by switching to a HPWH. Shown in Figure 4, this suggests that geographically a vast majority of the country would not benefit from the HPWH technology. The report goes on to say "[SWH] systems could be used in all U.S. locations; however, they need to be optimized for cold climates such that they yield sufficient savings to be worthwhile."[5] This indicates a need to design solar thermal collectors for cold climate zones.

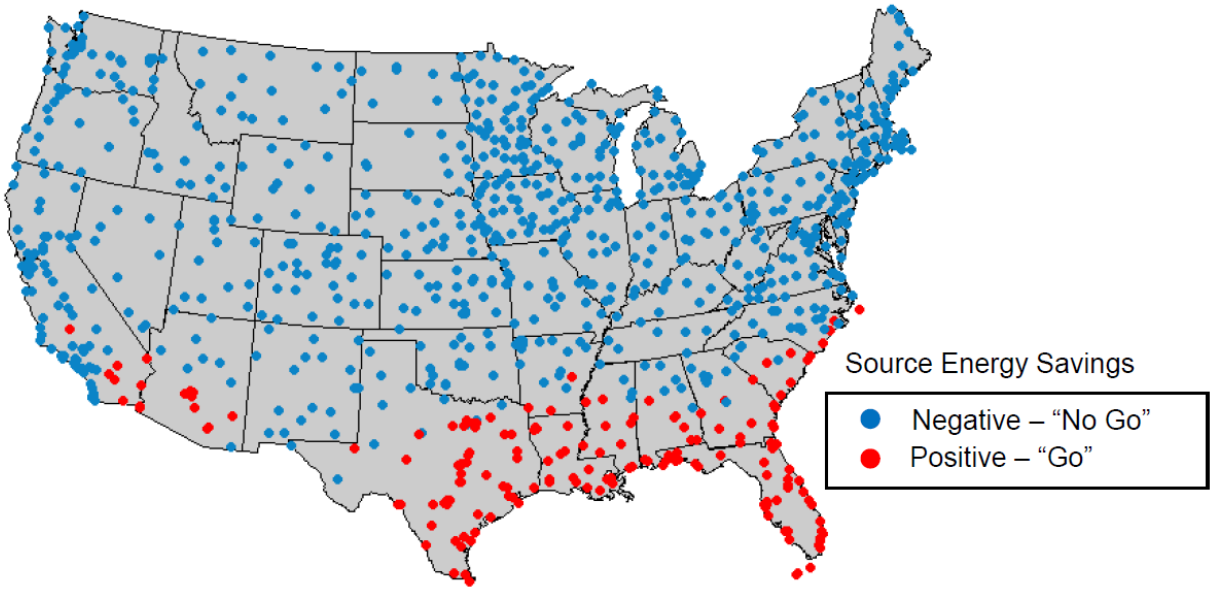

Figure 4. Go/No-Go Map for Heat Pump Water Heater Use

Manufacturer rating of solar collector designs is not comprehensive. Collector efficiency is evaluated after a panel has been constructed. Methods for certifying solar collector designs are outlined in the Solar Rating & Certification Corporation (SRCC) OG-100 standard "Test methods and minimum Standards for Certifying Solar Collectors"[6] and the American Society of Heating, Refrigerating and Air Conditioning Engineers (ASHRAE) standard 93-2010 "Methods of Testing to Determine the Thermal Performance of Solar Collectors."[7] To determine thermal performance, a collector is mounted to a test frame and is irradiated from a light source normal to its surface. This source is measured by a pyranometer. Irradiance, along with measured ambient conditions, fluid temperature change, and mass flow rate, is used to calculate a second order efficiency curve as a function of $\frac{T_{in}-T_{od}}{I}$. If the heat resistance equation, Eq. 1, is considered, then rearranging it shows that the independent variable used by manufacturers is analogous the overall thermal resistance of the system. The efficiency curve does not take into account the effect of different wind speeds since wind speed remains constant throughout the process.

$$q = \frac{\Delta T}{\sum R} \quad \textbf{(1)}$$

Certification also includes the calculation of an incident angle modifier. For this test the efficiency of the collector is found when the radiation source is at four different angles relative to the collector face. When scaled by the maximum efficiency which occurs at normal irradiance, the ratio of efficiencies create a modifier number as a function of angle. These data points are used to make a curve fit function which predicts the reduction in efficiency as the angle of the light source is changed. This test is representative of only the beam component of radiation and does not take into account the diffuse aspects of sunlight, nor does it take into account the changes in solar spectrum intensity encountered from variable air masses in actual installations. This method has led to the construction of plots such as the one shown in Figure 5 used to size solar collectors. They are an oversimplification of the physics taking place.

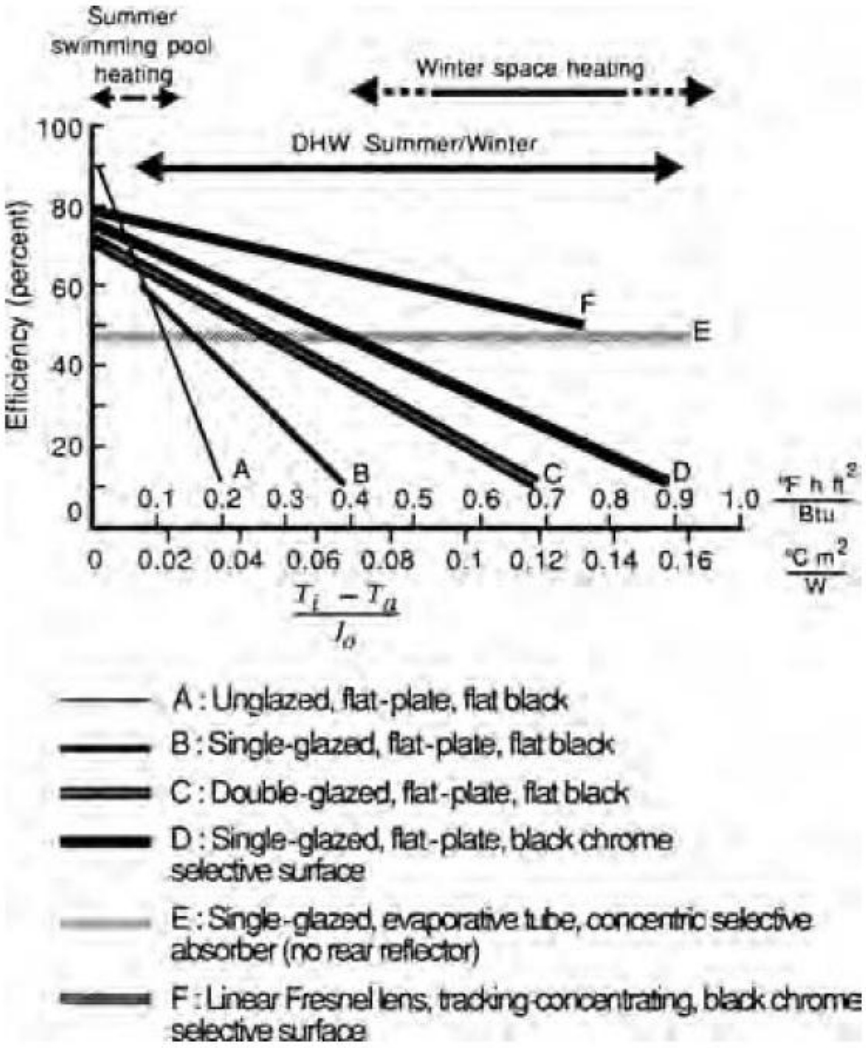

Figure 5. Sample Efficiency Curves for Various Collector Types

The most important aspect of a solar collector is how it interacts with the sun. By creating a heat transfer model which takes into account the solar properties of a collector, a simulation can be created to determine the performance of a particular design without the need for a prototype fabrication. Key parameters can be changed to quickly see the effects on the system to determine the best construction. One such piece of information is the angle between the Sun and collector as a function of geographical location and time. Chang[8] uses a formula to predict the incident angle of sunlight on a collector surface as well as the amount of time sunlight will be present on a collector surface. Such information

is critical in a simulation to accurately quantify the solar radiation absorbed by a collector. Also, because sunlight has different intensities at different wavelengths, radiometric properties must be taken as a function of wavelength. These properties can vary for the same material across wavelengths of the Sun[9]. Gueymard[10] demonstrates the calculation of "bulk optical properties," weighted averages of the radiometric properties across the solar spectrum. This calculation requires a measure of intensity of solar radiation at different wavelengths. Duffie and Beckman[11] state that these values can vary depending on a location's air mass, as shown in Figure 6.

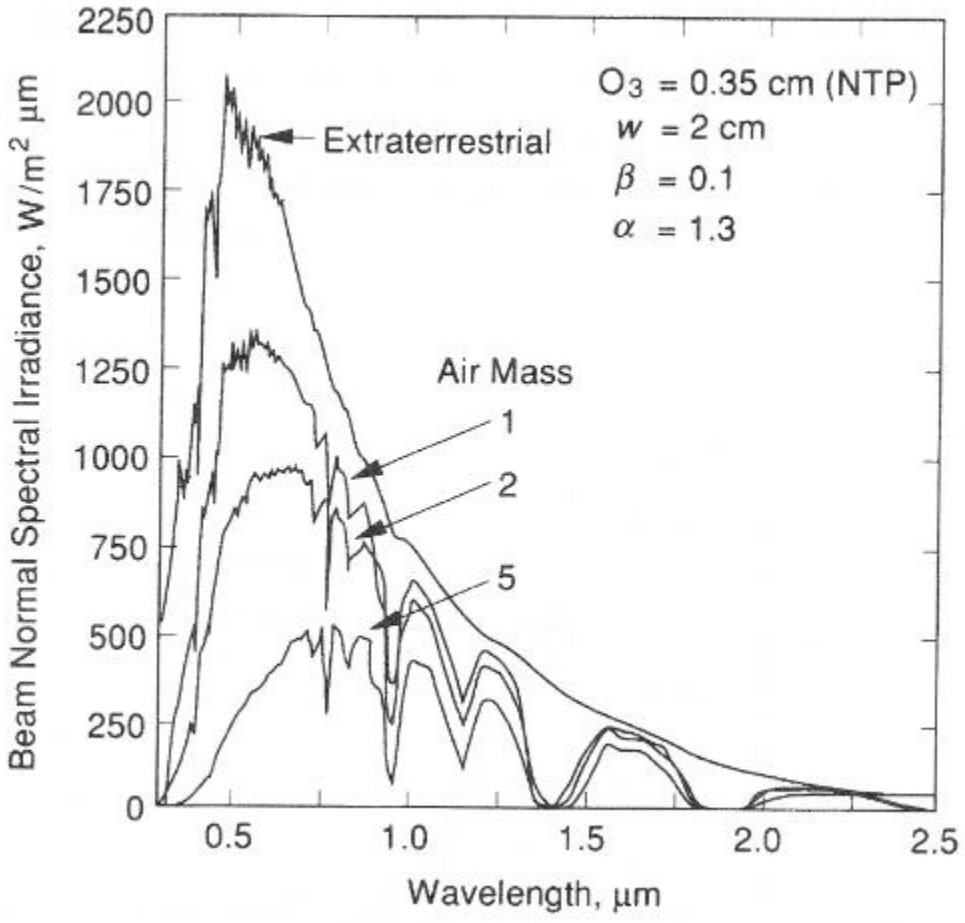

Figure 6. Spectral Beam Irradiance at Various Air Masses[11]

Other works have sought to create a thermodynamic model of solar collector heat transfer. Villar et al.[12] developed a transient, 3 dimensional transient model for both

serpentine and parallel flow solar collectors. Here the absorber plate was discretized with boundary conditions from the backside insulation and glass cover. The temperature of the glass cover was averaged. While time dependent, the solar radiation was a boundary condition, and did not take into account spectral properties or incident radiation. Wills[13] modeled a serpentine flow collector using the commercial software TRANSYS to evaluate the energy storage ability of SWHs in a full building simulation. Lund[14] calculated the 2 dimensional heat conduction across the absorber face for a serpentine collector of variable size. Each tube pass across the surface was separated on the plate into individual strips. Heat loss was taken to an ambient condition and solar radiation was considered a heat gain. However, this did not address the ability to calculate the solar flux that would reach the absorber surface for different construction types.

The goal of this work is not to replicate the previous heat transfer models. Instead it seeks to create the groundwork for a more detailed code. It will demonstrate the ability of serpentine flow flat plate solar collectors to be modeled in a 1 dimensional sense. The results of this model will be compared against field site data from an installation in an occupied home over different parts of a year.

The New Norris House is a design/build/evaluate project put forth by the University of Tennessee located in Norris, TN. Its purpose is to show an updated take on the planned community of Norris originally founded in 1933. This community was designed by the Tennessee Valley Authority (TVA) during the creation of the Norris Dam and was meant to serve as a model community to showcase the advantages of planned housing. The New Norris House sought to demonstrate a modern take on this idea. Led by student efforts, the home was designed with efficiency and sustainability as its main criteria, while still conforming to the architectural style common to the community. The New Norris House has won numerous awards for "design, pedagogy, and environmental performance, including the EPA P3 Award, the NCARB Prize for the Creative Integration of Research and Practice, the ACSA Design|Build Award, a RADA Merit Award, and an AIA Gulf States Award of Merit."[15] Figure 7 shows the completed home's exterior with the solar absorber panel marked.

Figure 7. The New Norris House[16]

Various energy efficient technologies are employed throughout the house. A Mitsubishi Variable Refrigerant Flow heat pump provides multi-zone conditioning, and an Energy Recovery Ventilator provides fresh air ventilation while reducing the load from outdoor air. The home also incorporates several passive energy technologies. There is a rainwater collection system that sanitizes captured rainfall for use as household greywater and irrigation. A solar water heating system transfers the Sun's energy to supplement and the home's water heating load. The New Norris House is currently in its evaluation phase. Various performance metrics are recorded, allowing for analysis and assessment of the individual technologies and overall performance of the whole home. This work will focus specifically on the solar water heater data as a means to validate the developed model.

The system used in the New Norris House was a commercially available residential indirect system manufactured by EnerWorks. It used a single absorber panel of dimensions 2.441m by 1.171m mounted 2.1° from horizontal and faces 22° West of South . It utilized a

50/50 % mix by volume of propylene glycol and deionized water as the working fluid. Other properties of this collector were known to a limited degree but considered confidential by the manufacturer and have been asked to be left out of this work. While some parameters were available from the collector's certification document, others had to be assumed. For example, the exact design of the absorber plate was unknown. It was assumed that the coolant tube was welded to the top-side of the absorber plate. The electronic controller for the system internally monitored numerous system temperatures. It used this data to provide protection to the system, such as stopping the working fluid pump if the stored water temperature was too high or shutting itself off if the collector was not hot enough to effectively transfer heat to the water storage tank. This means that the system is not in continuous operation. In addition to the collector and controller, the system is comprised of an external heat exchanger that routes working fluid and stored water. Figure 8 is a depiction of the indirect water heating system as it appears inside the New Norris House.

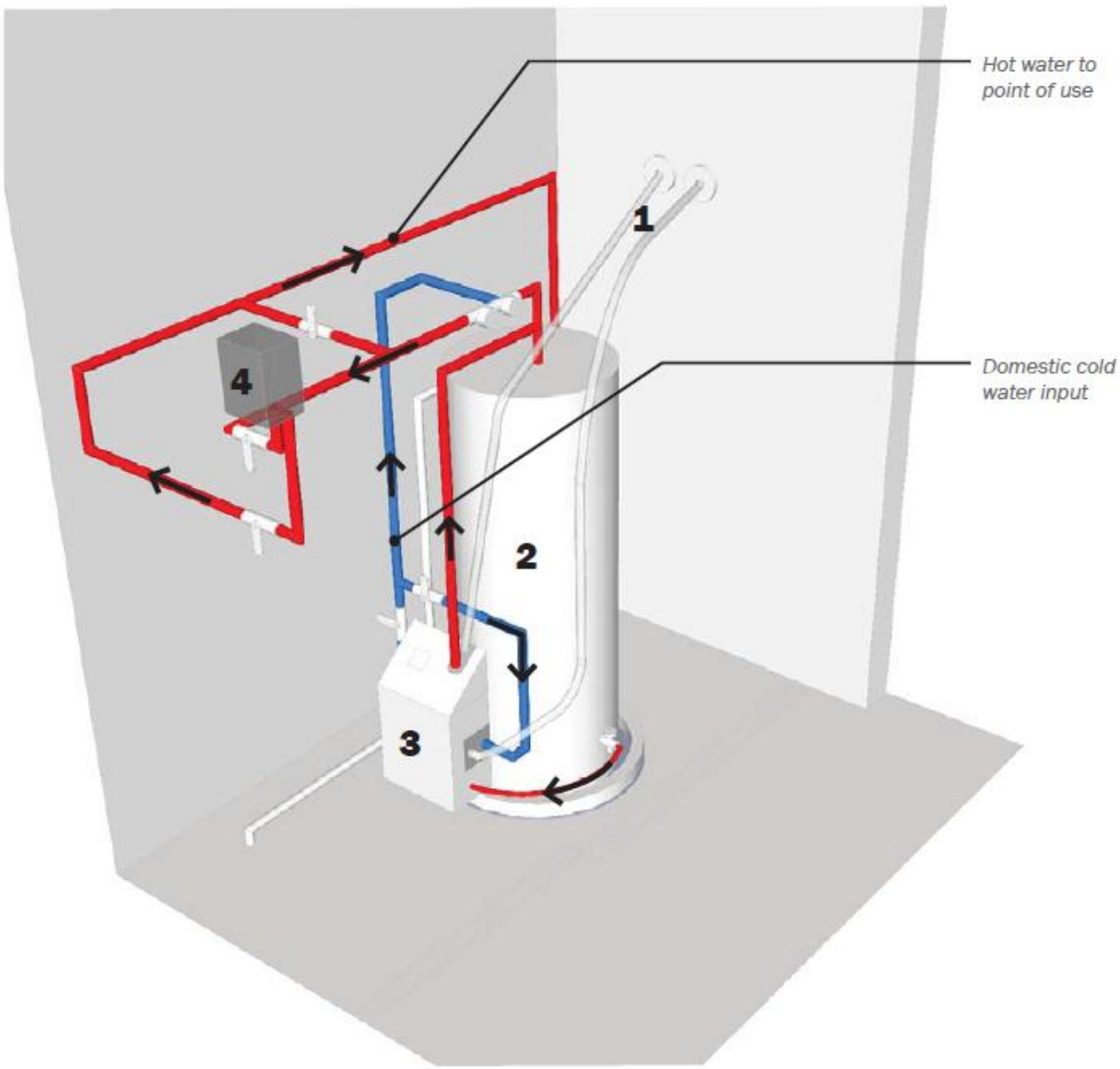

1 Glycol lines to 2.88m² Enerworks solar hot-water panel on roof
2 Rheem 80 gallon storage tank (no elements)
3 Eneryworks Energy Pack (heat exchanger and system controller)
4 11.8kW Eemax instantaeous thermostatic water heater

Figure 8. New Norris House Water Heating Configuration[17]

Chapter 2: Heat Transfer Model

2.1 Scope and Discretization

The first thing that needed to be decided upon was the scope of the model. For this phase of the model the irradiance was assumed normal to the collector so that radiometric properties would be constant, and therefore radiometric computations not required as a function of solar wavelength or incident angle. This greatly simplified the calculations as the spectral properties of the glass could be fixed. As a consequence of this assumption however, irradiance field data is only valid close to solar noon. This immediately limits the model from being a simulation; it cannot be run for continuous days of data at a time.

The derivations presented are shown for a single glass pane only. However, the mathematical techniques developed for this code may be applied to develop equations for multiple glazings. This model also assumes a closed air cavity between the glass and absorber plate with a layer of insulation between the absorber plate and the exterior aluminum housing.

The model accepts a wide variety of inputs. The user may edit a text file to specify the collector size, tilt angle, working fluid and its composition, pipe diameter and length, and radiometric properties of the glass and absorber. In addition to the physical properties of the collector, boundary conditions are required to complete the mathematical description. These include outdoor air temperature, incoming fluid temperature, working fluid flow rate, and the normal irradiance. For validation, these came from the field data. For the bottom of the collector, heat transfer is due to natural convection to an airstream taken as the outdoor air temperature. Since the house roof temperature is not available, underside radiation is neglected.

The primary output of the model is the working fluid outlet temperature. The change of fluid temperature, a calculated specific heat, and a known flow rate determine the heat transferred into the tank heat exchanger. Assuming no losses in the heat exchange to the water, this allows for the calculation of supplemental heat delivered to the tank. The

model does not take into account how this affects the overall energy stored in the tank or water supply temperature. As a consequence of the calculations involved in the model, the temperatures of the different components within the panel are also calculated.

The model is built upon first principles of heat transfer. The primary equation used in this model is the energy conservation equation shown in Eq. 2. The system was assumed to be at quasi-steady state. At each 15 minute interval for which data was available, boundary conditions were applied and the system was solved with Gauss-Seidel iteration to equilibrium.

$$\dot{E}_{in} + \dot{E}_{gen} = \dot{E}_{out} \quad \textbf{(2)}$$

The system was simplified to one dimensional heat transfer vertically through the glass cover. This was justified by assuming the ambient air temperature and insolation were uniform across the surface of the collector, and the metal piping and absorber surface caused negligible planar heat transfer. The serpentine flow pattern was therefore stretched into a continuous length. A top-down view of the actual and assumed geometry are shown in Figures 9 and 10 below, not to scale. Six temperatures were calculated within the system and are listed in Table 1 and shown in Figure 11.

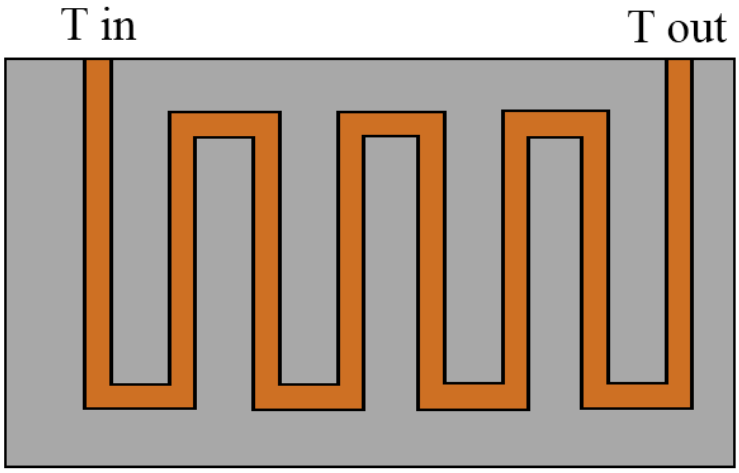

Figure 9. Actual Collector Serpentine Flow Pattern

Figure 10. Flow Pattern as Seen by Model

Table 1. Calculated Temperature Locations

Temperature Variable	Location
T_1	Top of Glass
T_2	Bottom of Glass
T_3	Absorber Plate/Pipe
T_4	Heat Transfer Fluid Out
T_5	Bottom of Insulation
T_6	Bottom of Absorber Housing

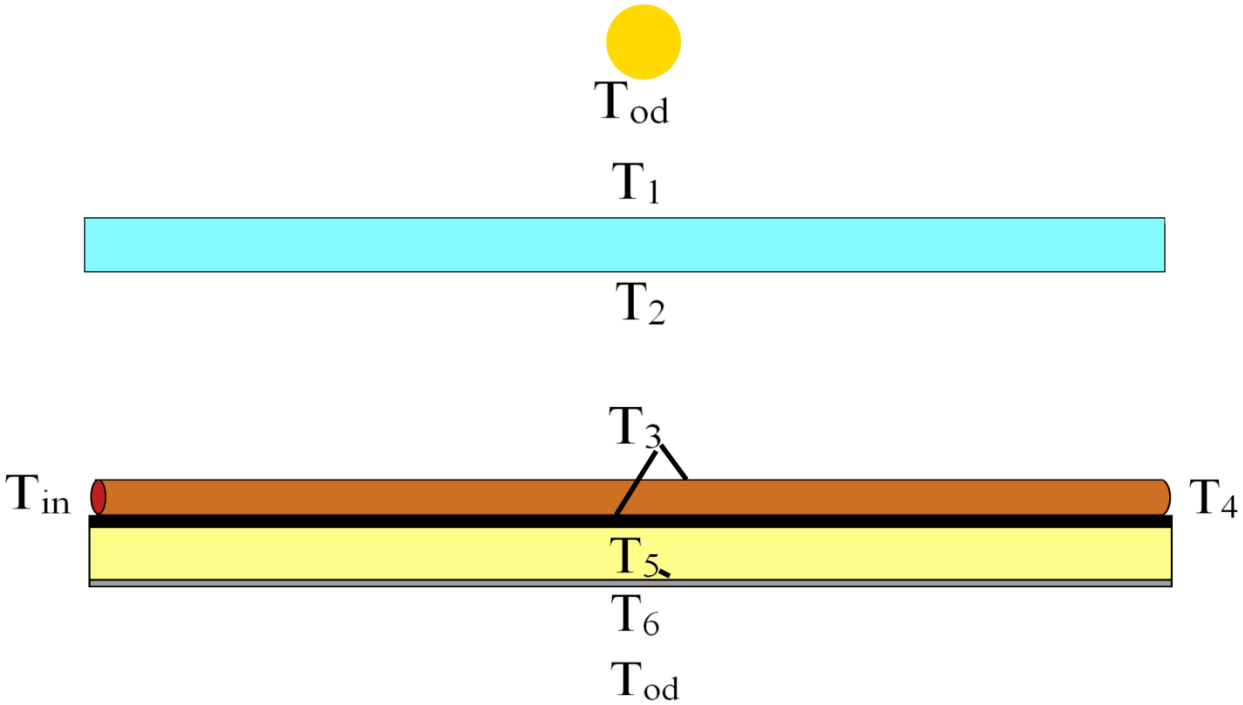

Figure 11. Temperature Variable Locations inside Collector

It is recognized the absorber is not truly one dimensional in heat transfer. The pipe running across the absorber plate experiences a significant temperature change. For this reason, the pipe, and thus the collector, was divided into numerous subsections of smaller length. In the first subsection, the inlet fluid temperature was taken as an input. The areas over which the modes of heat transfer acted were scaled down by the number of substeps, and the equations in each interval were allowed to converge. This yielded an outlet temperature of the heat transfer fluid, which was then used as the inlet temperature for the next group of equations. Calculating the heat transfer across the full length of pipe would result in neither a constant flux nor a constant temperature wall condition, but breaking the pipe into multiple smaller sections permitted better estimation of the working fluid's temperature exiting a control volume.

Because the fluid temperature was expected to change by an appreciable amount along the length of the pipe, the temperature distributions throughout each subsection were expected to change, which affected heat transfer between the absorber plate and the glass cover plate. However, the convection coefficient correlations depended on the full size of the cavity. Basing these coefficients on numerous smaller cavities would not yield the same results because of the change in aspect ratios. For this reason, average temperatures were calculated, such as in Villar[12], and used in calculating the convection coefficients throughout the panel. An arithmetic average of all the calculated temperatures at each layer was used as one of the inputs to calculate the film temperatures. Since the initial average temperatures were taken as guesses, after the final subsection converged, the sets of equations were rerun with the updated values for average layer temperatures.

2.2 Convection and Radiation Heat Transfer Coefficients

On the top surface of the collector mixed convection and radiation heat transfer were modeled. The radiation potential was between the glass temperature T_1 and the outdoor temperature T_{od}. Night sky temperature data was unavailable. The view factor to the sky was taken to be 1. The temperatures and glass emissivity were combined to form a

radiation heat transfer coefficient $h_{ro,1}$ in Eq. 3. Since a layer may have different emissivities on either side of its surface, the notation $\varepsilon_{i,j}$ is used to index surfaces, where *i* represents the layer number and *j* indicates the surface, going from top to bottom. Therefore $\varepsilon_{1,1}$ represents the emittance of the glazing facing the sky while $\varepsilon_{1,2}$ would be the emittance of the glazing facing the absorber plate.

$$h_{ro,1} = \sigma\varepsilon_{1,1}(T_1 + T_{od})(T_1^2 + T_{od}^2) \quad \textbf{(3)}$$

Both natural and mixed convection were assumed on the outer surface. The thermal properties of air were evaluated at to film temperature T_f by the method described in ISO 15099[18], shown in Eq. 4. The thermodynamic properties for air were calculated from 4th order curve fits from National Institute of Standard and Technology (NIST) routines.

$$T_f = T_{od} + .25(T_1 - T_{od}) \quad \textbf{(4)}$$

The forced convection coefficient was taken from Incropera et al.[19] across a flat plate shown in Eq. 5 and 6, accounting for laminar and turbulent flow. The Nusselt number and heat transfer coefficients were the average value across the plate. When used to find heat transfer, the flux was multiplied by a scaled area equal to the total collector area divided by the number of substeps taken. Transition from laminar to turbulent was assumed to occur at $Re_{x,c} = 500{,}000$. The Reynolds number calculation used the longer dimension of the collector W as its characteristic length.

$$Re_W < 5E5 \qquad \overline{Nu}_{forced} = .664 Re_W^{.5} Pr^{1/3} \quad \textbf{(5)}$$

$$Re_W \geq 5E5 \quad \overline{Nu}_{forced} = \left(0.037 Re_W^{4/5} - 871.323\right) Pr^{1/3} \quad \textbf{(6)}$$

The natural convection coefficient came from ISO 15099 for free convection on an inclined surface[18]. The characteristic length W in the calculation of Ra_W was the length of the inclined slope, which was the longer panel dimension.

$$Ra_W = \frac{g|\Delta T|\left(\frac{1}{T_f}\right)W^3\rho^2 c_p}{k\mu} \textbf{ (7)}$$

$$\overline{Nu}_{nat} = .13Ra_W^{1/3} \textbf{ (8)}$$

For mixed convection the Nusselt numbers were combined as detailed in Incropera et al.[19] and the convection coefficient $\bar{h}_{co,1}$ was calculated as shown in Eq. 9 and 10. The mixed convection and radiation coefficients were added together for a combined heat transfer coefficient on the outer surface $\check{h}_{o,1}$ in Eq. 11.

$$\overline{Nu}_{mix} = \left[(\overline{Nu}_{nat})^{7/2} + (\overline{Nu}_{forced})^{7/2}\right]^{2/7} \textbf{ (9)}$$

$$\bar{h}_{co,1} = \frac{\overline{Nu}_{mix} * k}{W} \textbf{ (10)}$$

$$\check{h}_{o,1} = h_{ro,1} + \bar{h}_{co,1} \textbf{ (11)}$$

Inside the solar panel was an enclosed air cavity that separated the glass from the absorber plate. Since there was a finite space between the glass and the absorber, there is some view factor between the top and bottom plate. However, because the sides of the collector are assumed adiabatic, all energy radiated to them is re-radiated; therefore the view factor between the bottom of the glass and the top of the absorber plate was taken as 1. This view factor was used in the equation for radiation heat transfer coefficient between the pane and absorber in Eq. 12, where σ is the Steffan-Boltzman constant and $\varepsilon_{i,j}$ are the emissivities of the glass or absorber plate.

$$h_{r2,3} = \sigma(T_2 + T_3)(T_2^2 + T_3^2)\Big/\left[\frac{1-\varepsilon_{1,2}}{\varepsilon_{1,2}} + \frac{1}{F_{2,3}} + \frac{1-\varepsilon_{2,1}}{\varepsilon_{2,1}}\right] \textbf{ (12)}$$

Holland's correlation[19], shown in Eq. 13, was used to calculate the natural convection in an enclosed, inclined cavity. Since the space was enclosed there was no forced convection. This correlation included condition that the tilt angle τ of the enclosed space be less than a critical tilt angle τ^* for the cavity's aspect ratio. The ratio was defined as the length of the inclined surface W up which the air would convect divided by the gap space H_g between the top and bottom of the cavity. Additionally, if the values inside the brackets denoted with a dot produced a negative value, the value of the bracketed terms was taken as zero. Holland's correlation is only valid if the bottom temperature is greater than the top temperature, allowing buoyancy forces to circulate the fluid. If this is not true, a different correlation must be used. Due to the constraints of this model, primarily that data is taken near solar noon, the absorber temperature T_3 will always be warmer than bottom of glass temperature T_2. The natural convection and radiation coefficients were again combined to provide a combined heat transfer coefficient inside the cavity.

$$\overline{Nu}_{H_g} = 1 + 1.44\left[1 - \frac{1708}{Ra_{H_g}\cos\tau}\right]^{\cdot}\left[1 - \frac{1708(\sin 1.8\tau)^{1.6}}{Ra_{H_g}\cos\tau}\right] + \left[\left(\frac{Ra_{H_g}\cos\tau}{5830}\right) - 1\right]^{\cdot} \quad \textbf{(13)}$$

$$where\ \frac{W}{H_g} \geq 12, \quad 0 < \tau < \tau^*$$

Extruded polystyrene insulation was installed around the inner perimeter of the assembly, and the sides of the solar panel were assumed adiabatic. They provided a relatively small area for heat transfer to occur. Instead all heat transfer was channeled through the absorber plate at temperature T_3. The properties of the water/glycol mixture were calculated using 5th order curve fits produced by the Engineering Equation Solver (EES) program and were a function of both temperature and the mixture's weight percent. The properties were evaluated at the average of the fluid inlet and outlet temperatures of the pipe section.

The internal convection was undoubtedly the most important aspect of this model. The internal flow heat transfer coefficient was an order of magnitude greater than the natural, forced, and radiation heat transfer coefficients. Thus the model was dominated by this value. Because the working fluid flowed in a continuous loop, the fluid was

hydrodynamically fully developed. However, upon entering the solar collector, it would begin to heat. For this reason, there was some thermal entry region for the fluid. Additionally, since the fluid could be either laminar or turbulent depending on the flow rate and viscosity of the fluid entering the collector, both situations had to be accounted for.

The first case examined was the laminar case. For the purposes of this code, laminar flow was assumed for $Re < 3000$. A piecewise function for local Nusselt number was presented in Rohsenow et al.[20] for laminar internal convection in the thermal entry region and shown in Eq. 14 in terms of a dimensionless length x^+, shown in Eq. 15. The Nusselt number of thermally fully developed laminar flow is 4.364[20]. Eq. 14 asymptotically approaches this value for large values of x^+.

$$Nu = \begin{cases} 1.64(x^+)^{-1/3} - 1 & for\ x^+ \leq 0.0001 \\ 1.64(x^+)^{-1/3} - 0.5 & for\ 0.0001 \leq x^+ \leq 0.003 \\ 4.364 + 12.33(10^3 x^+)^{-0.506} e^{-20.5x^+} & for\ x^+ \geq 0.003 \end{cases} \textbf{(14)}$$

$$x^+ = \frac{(2x/D)}{(RePr)} \textbf{(15)}$$

Turbulence must also be considered. Figure 12 from Çengel[21] shows the Nusselt number of developing turbulent flow as a function of length divided by inner diameter and a constant Prandtl number for both constant wall temperature and heat flux. The type of heat transfer present at the wall has little effect on the value, with the constant flux case being slightly higher in the developing region. Unlike laminar flow, the behavior of the Nusselt in the fully developed region is a function of Reynolds and Prandtl number. For the collector examined in this model, and assuming a worst-case Reynolds number of 2E5, the flow should be thermally fully developed by 0.89 cm. Based on field data, that high of a Reynolds number would be unrealistic in a solar collector. Instead taking Reynolds as 10,000, turbulent flow should be fully developed by 2.2 cm. Assuming 50 substeps, a number determined in Chapter 4, the first length of pipe will be only 30 cm, making this developing section a moot point.

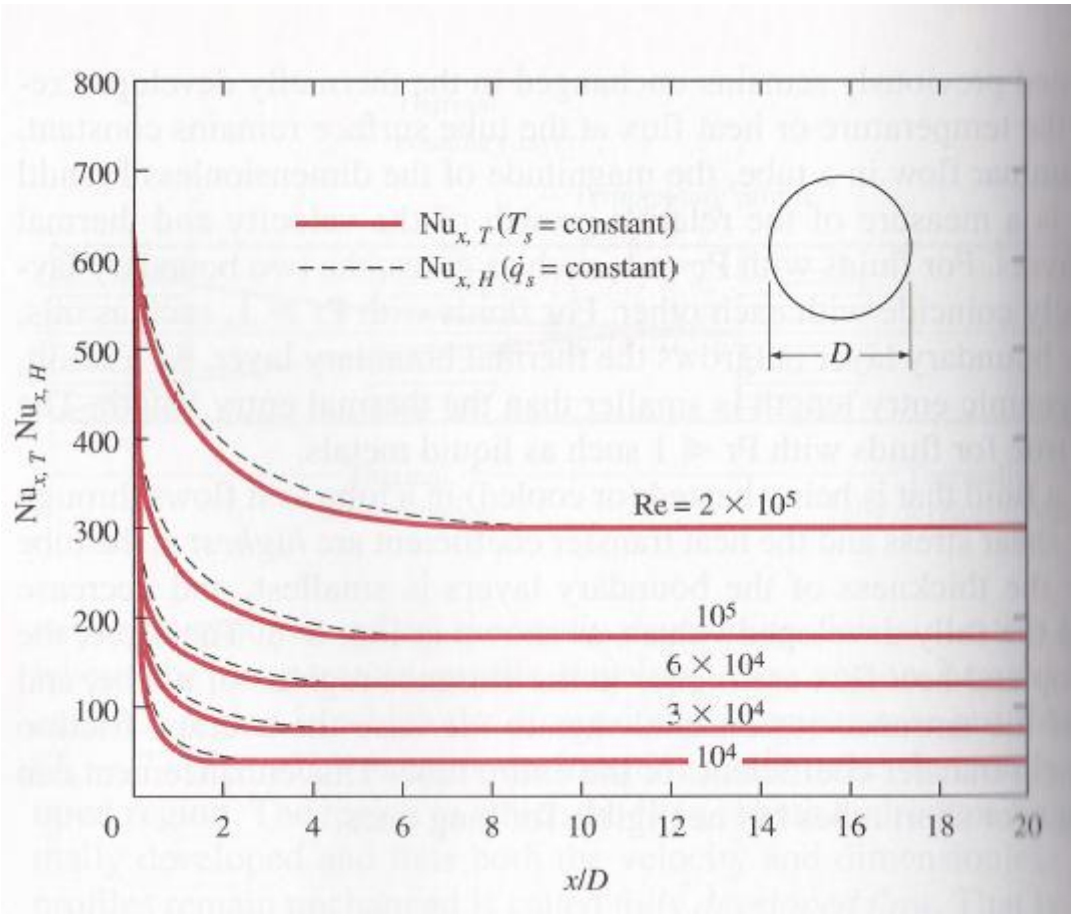

Figure 12. Internal Turbulent Convection

Nonetheless, thermally developing turbulent flow heat transfer was developed to make the code more versatile for potential flow scenarios. Roshenow et al. provide eigenvalue solutions for several cases of turbulent flow entry region at distinct Reynolds and Prandtl numbers. The analytical solutions for the pairs Pr=0.7/Re=50,000, Pr=10/Re=50,000, Pr=0.7/Re=100,000, and Pr=10/Re=100,000 were given in the text. Since the Prandtl numbers would range from approximately 7 for water and 25 for a propylene glycol mixture and the Reynolds number would be much less than 50,000, an interpolation/extrapolation method was used to predict the Nusselt numbers for thermally developing flow based on those solutions.

If the working fluid was determined to be thermally developing turbulent flow, the four eigenvalue solutions presented above were solved for the particular x^+. Then, for both

the Re=50,000 and 100,000 cases, Nusselt numbers were found by interpolation for the actual Prandtl number using Eq. 16 and 17 below. The Nusselt numbers have subscripts $Nu_{a,b}$, where "a" denotes the Pr and "b" denotes the Re. If denoted with either Pr or Re, it means the actual calculated value of the fluid.

$$Nu_{Pr,50k} = \frac{Pr-.7}{10-.7}\left(Nu_{10,50k} - Nu_{0.7,50k}\right) + Nu_{0.7,50k} \quad \textbf{(16)}$$

$$Nu_{Pr,100k} = \frac{Pr-.7}{10-.7}\left(Nu_{10,100k} - Nu_{0.7,100k}\right) + Nu_{0.7,100k} \textbf{(17)}$$

Doing this theoretically yields a pair of Nusselt numbers specific to the actual Prandtl number, but evaluated at distinct Reynolds numbers. To account for the actual Reynolds number, these points were linearly extrapolated using Eq. 18 below to mimic the form $Nu = m * Re + b$.

$$Nu_{Pr,Re} = \left(\frac{Nu_{Pr,100k} - Nu_{Pr,50k}}{100{,}000 - 50{,}000}\right) Re + 2Nu_{Pr,50k} - Nu_{Pr,100k} \quad \textbf{(18)}$$

For fully developed turbulent flow, the Nusselt number was presented in Incropera et al.[19] for Prandtl ranging from 0.5 to 2000 and is given in Eq. 19, where f if the friction coefficient, defined in Eq. 20.

$$Nu = \frac{(f/8)(Re-1000)Pr}{1+12.7(f/8)^{.5}(Pr^{2/3}-1)} \quad \textbf{(19)}$$

$$f = (.790 \ln Re - 1.64)^{-2} \quad \textbf{(20)}$$

The absorber plate was designed so that it would be the hottest component of the absorber during sunny periods. Therefore there was heat loss from the absorber panel to the shaded area of the roof. Underneath the absorber plate was a layer of rock-wool insulation and the thin aluminum casing of the panel. Past the casing were a shaded, open airspace and then the roof. The conductive resistance of the insulation and casing and

convection resistance of the bottom side were calculated to find the overall resistance to heat flow between T_3 and T_{od} in Eq. 21. This resistance allowed for the calculation of heat loss through the underside of the collector.

$$\sum R = \frac{L_{ins}}{k_{ins}} + \frac{L_{metal}}{k_{metal}} + \frac{1}{\bar{h}_{c,sh}} \textbf{(21)}$$

The convection under the collector was predicted using Azevedo and Sparrow's correlation for natural convection in an open-ended inclined channel[22]. It is presented in Eq. 22, and is based on the Rayliegh number in Eq. 23, where *Ra* is defined previously in Eq. 7. Here H_{az} is the gap between the collector and the roof and W is the length of collector along the flow path, taken to be the longer dimension of the collector.

$$\overline{Nu}_{c,sh} = .673\left(\frac{H_{az}}{W} Ra_{az}\right)^{0.3} \textbf{(22)}$$

$$Ra_{az} = Ra_{H_{az}} * (T_6 - T_{od}) \sin(\pi \frac{90-\tau}{180}) \textbf{(23)}$$

2.3 Shortwave Radiation

In addition to the standard longwave radiation present between bodies, the use of glass necessitated the calculation of shortwave effects. For these calculations, the glass radiometric properties are required. The properties are the reflectance Rf and absorbtance Ab of both sides of the glass and the total glass transmittance Tr. The net radiation method[23] was used to relate the solar radiation to longwave heat transfer.

In this model the Sun's energy was taken as independent of wavelength. The properties for the glass were taken at a weighted average across the solar spectrum. The transmittance of the glass was specified in the glass manufacture's literature; reflectance information was not available and was assumed to be that of clear glass. Part of the Sun's energy is transmitted through the glass, part is reflected off the glass, and the rest must be

absorbed within the glass. This relationship is described in Eq. 24. Since any glass may have different properties on either side, the relationship must be satisfied for each side separately.

$$Tr + Rf + Ab = 1 \textbf{ (24)}$$

This model only deals with a single glass pane on the absorber panel; multiple panes may also be incorporated by the same logic. As the absorber plate also interacts with transmitted shortwave energy, it may be treated, with respect to shortwave radiation, as a glass pane with a transmittance of zero. The reflectance of the absorber plate was specified by the manufacturer, thus providing its absorbtance. The shortwave element of heat transfer occurs independently of temperature and flow rate boundary conditions and is described using a special notation. The notation $q_{i\ a,b}$ is used to describe the different shortwave intensities in units of W/m^2. Here "i" denotes that the energy is being transferred "into" a particular plate. "a" denotes which plate is being referenced, where 1 is the top glass plate and increases down the stack. "b" denotes which side of the plate is being referenced, where 1 means the top of the plate and 2 means the bottom. This notation can be used interchangeably for convenience with an "o" in place of "i" to indicate that energy is instead leaving the indexed surface. Figure 13 shows the shortwave elements of heat transfer present within a single pane absorber panel.

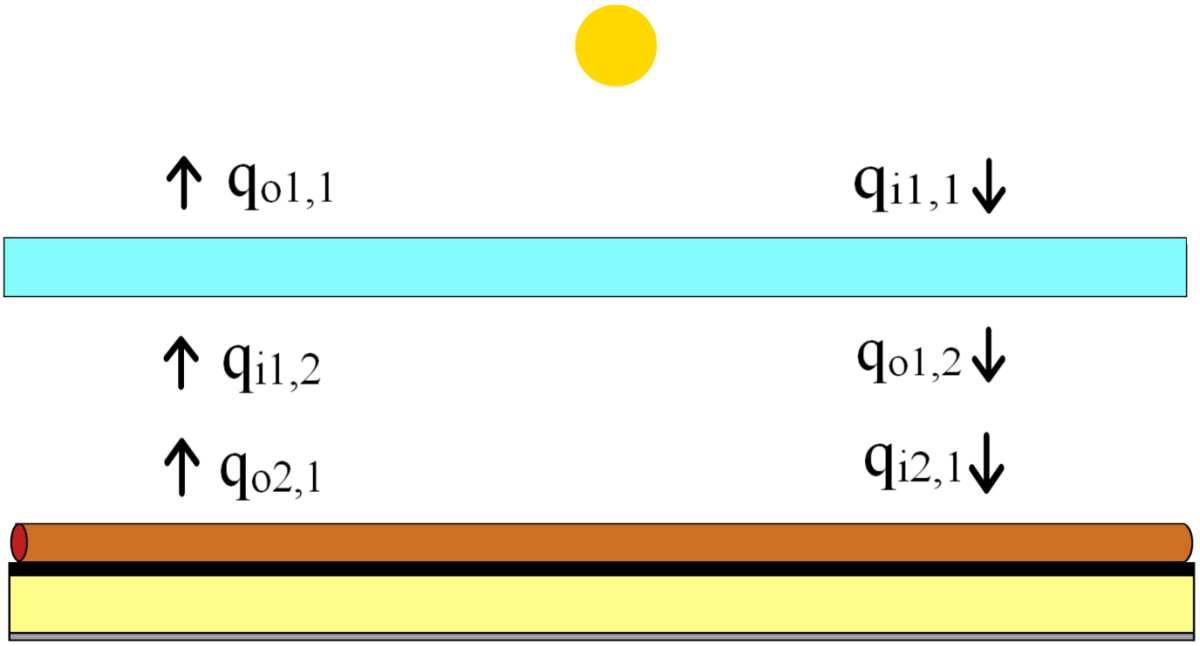

Figure 13. Shortwave Heat Transfer

The incoming radiation on the top plate, $q_{i\ 1,1}$, is from the Sun, thus it is equal to the normal irradiance I. There are two components of energy leaving the top plate. One is the portion of I that is reflected by the top pane of glass. The second is the portion of shortwave radiation from the absorber plate that gets transmitted through the top pane. Together these comprise $q_{o\ 1,1}$. Such logic may be carried out for the remainder of the surfaces, noting that $q_{o\ 1,2} = q_{i\ 2,1}$ and $q_{o\ 2,1} = q_{i\ 1,2}$. This forms a system of equations 25 through 30 as follows.

$$q_{i\ 1,1} = I \quad \textbf{(25)}$$

$$q_{o\ 1,1} = I * Rf_{1,1} + q_{i\ 1,2} * Tr_1 \quad \textbf{(26)}$$

$$q_{o\ 1,2} = I * Tr_1 + q_{i\ 1,2} Rf_{1,2} \quad \textbf{(27)}$$

$$q_{i\ 1,2} = q_{o\ 2,1} \textbf{ (28)}$$

$$q_{i\ 2,1} = q_{o\ 1,2} \textbf{ (29)}$$

$$q_{o\ 2,1} = q_{i\ 2,1} * R_{f2,1} \textbf{ (30)}$$

The system may be solved numerous ways to yield the respective portions of normal irradiance entering and leaving each surface as functions of I and the radiometric properties Tr and Rf. When used in energy balances, these values have units of $\frac{W}{m^2}$ and are treated as additional flux terms. Note that these shortwave radiation values are independent of temperature and other forms of heat transfer. They depend entirely upon the properties of the materials and solar irradiance, and thus are not treated as unknowns. Note that the portion of shortwave radiation that is not reflected or transmitted is what is absorbed. This becomes the portion of shortwave energy that gets transformed into longwave energy through a generation term. This is explained further in Chapter 3.

Chapter 3: Calculations

3.1 Energy Balances

Energy balances were taken at various locations within the absorber panel. Initial guesses were needed for the six temperature values. As T_{od} and I were both known boundary conditions, T_1 was calculated first. Using the initial guesses, an energy balance was rearranged and used to calculate an updated value of T_1. This updated value was passed along to the equation for T_2, and then so on until all temperatures had been calculated. Then the process was repeated with these new, more accurate temperature values, making the solution technique a Gauss-Seidel method.

First the top glass plate was examined. Figure 14 shows the heat transfer modes present on the glass. $\dot{E}_{in}$ terms consisting of normal irradiance, reflected shortwave energy from the absorber plate, and natural convection and radiation in the panel's cavity space. A radiation heat transfer coefficient was used and the convection and radiation terms were summed to create the combined heat transfer coefficient $\check{h}_{2,3}$. $\dot{E}_{out}$ terms were the remaining shortwave components and mixed convection and radiation to the environment. This mixed convection coefficient was summed with the external radiation coefficient to form the combined heat transfer coefficient $\check{h}_{o,1}$. Energy rate in and energy rate out were equated in Eq. 31 and rearranged in terms of T_1 in Eq. 32.

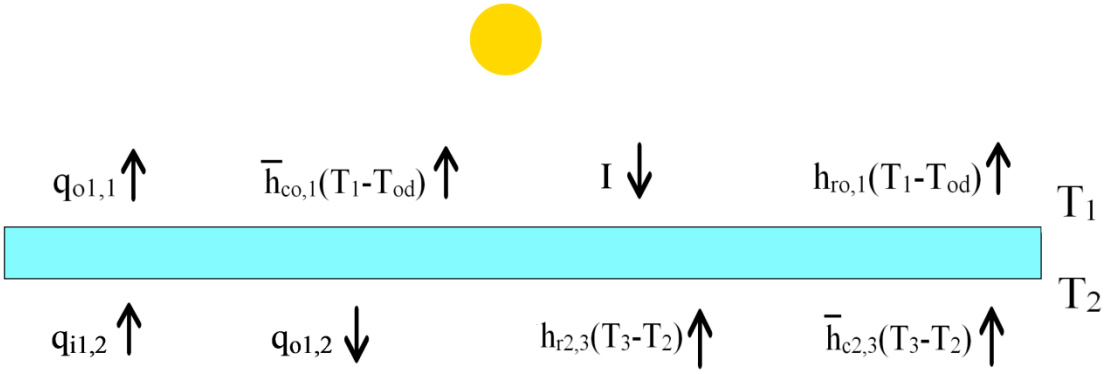

Figure 14. Top Pane Energy Balance

$$A_g\left[q_{i\,1,1} + q_{i\,1,2} + \check{h}_{2,3}(T_3 - T_2)\right] = A_g\left[q_{o\,1,1} + q_{o\,1,2} + \check{h}_{o,1}(T_1 - T_{od})\right] \textbf{(31)}$$

$$T_1 = \frac{q_{i\,1,1}+q_{i\,1,2}+\check{h}_{o,1}T_{od}+\check{h}_{2,3}(T_3-T_2)-q_{o\,1,1}-q_{o\,1,2}}{\check{h}_{o,1}} \textbf{(32)}$$

For T_2 the top pane was again examined. An energy balance is conducted on the pane, where flux through the top and bottom surfaces were considered, shown in Figure 15. Because the pane absorbed part of the shortwave radiation, these two fluxes were not equivalent. Here the temperature profile of the glass was calculated in Eq. 33 and assumes heat generation occurring as short-wave radiation that is uniformly absorbed into the glass as described in Eq. 34. The energy balance was used to quantify and relate short- and long-wave radiation heat transfer. The energy balance was integrated twice with T_1 and T_2 taken as boundary conditions. This produces temperature as a function of glass depth in Eq. 35.

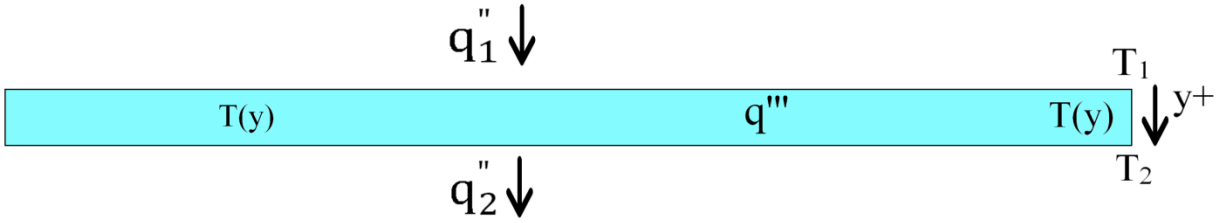

Figure 15. Top Pane Temperature Profile

$$k\frac{d^2T}{dx^2} + q''' = 0, \quad y(0) = T_1, \quad y(L) = T_2 \textbf{ (33)}$$

$$q''' = \frac{q_{i\,1,1} * Ab_{1,1} + q_{i\,1,2} * Ab_{1,2}}{L_g} \textbf{ (34)}$$

$$T(y) = \frac{-q'''y^2}{2k_g} + \left[\frac{(T_2 - T_1)}{L_g} + \frac{q'''L_g}{2k_g}\right]y + T_1 \textbf{ (35)}$$

Taking the first derivate of Eq. 35 and recognizing that by Fourier's Law it is equivalent to the negative of flux divided by thermal conductivity produces Eq. 36. Evaluating this equation at $y = 0$, the top surface, and recognizing that the flux term now becomes the long wave radiation on the top surface allows this equation to be rearranged for T_2 in terms of known values and recently updated T_1 properties in Eq. 37.

$$\frac{dT(y)}{dy} = -\frac{q'''y}{k_g} + \frac{T_2 - T_1}{L_g} + \frac{q'''L_g}{2k_g} = -\frac{q(y)''}{k_g} \textbf{ (36)}$$

$$T_2 = T_1 - \frac{L_g}{k_g}\left[\check{h}_{o,1}(T_{od} - T_1) - \frac{q_{i\,1,1} * Ab_{1,1} + q_{i\,1,2} * Ab_{1,2}}{2}\right] \textbf{ (37)}$$

The absorber panel not only had radiation and convection heat loss to the top pane, but also internal convection through the pipe and heat loss through the underside insulation as described in Figure 16. Since the outdoor air temperature was a boundary condition, the overall heat transfer resistance to the bottom side of the collector was calculated so that the heat transfer potential would be between T_3 and T_{od}. The pipes through which the fluid flowed were copper and therefore assumed to be at T_3. The internal pipe convection was related to the change in fluid temperature as shown in Eq. 38. Calculating an energy balance on the absorber plate yields Eq. 39, which was rearranged for the variable of interest T_3 in Eq. 40.

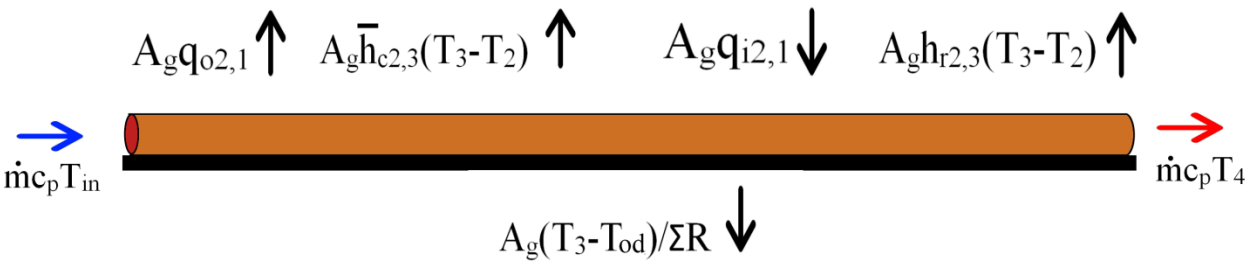

Figure 16. Absorber Plate Energy Balance

$$h_{int}A_i(T_4 - T_3) = \dot{m}c_p(T_4 - T_{in}) \textbf{ (38)}$$

$$A_g(q_{i\,2,1}) = A_g\left[q_{o\,2,1} + \check{h}_{2,3}(T_3 - T_2) + {}^{(T_3 - T_{od})}/_{\sum R}\right] + \dot{m}c_p(T_4 - T_{in}) \textbf{ (39)}$$

$$T_3 = \frac{A_g(q_{i\,2,1} - q_{o\,2,1} + \check{h}_{2,3}T_2 + {}^{T_{od}}/_{\sum R}) - \dot{m}c_p(T_4 - T_{in})}{A_g(\check{h}_{2,3} + {}^{1}/_{\sum R})} \textbf{ (40)}$$

The internal convection was assumed to take place between the pipe temperature T_3 and the section's outlet temperature T_4. The heat transfer from the pipe to absorber was locked to the energy delivered to the fluid with Eq. 38, and the outlet temperature was solved by rearranging to form Eq. 41, where A_i is the pipe's surface area.

$$T_4 = \frac{\dot{m}c_p T_{in} + h_{int} A_i T_3}{\dot{m}c_p + h_{int} A_i} \textbf{(41)}$$

With the value of T_3 updated, a boundary condition of T_{od}, and the values of thermal resistance, a loss term for the heat flux out of the bottom of the panel, q''_{loss}, was calculated in Eq. 42. Since the problem is at steady-state and no generation is taking place, the flux is constant throughout the bottom of the absorber. This allows T_5 and T_6 to be calculated in Eq. 43 and 44 in terms of q''_{loss}.

$$q''_{loss} = \frac{T_3 - T_{od}}{\sum R} \textbf{(42)}$$

$$T_5 = T_3 - q''_{loss} \frac{L_{ins}}{k_{ins}} \textbf{(43)}$$

$$T_6 = T_5 - q''_{loss} \frac{L_{met}}{k_{met}} \textbf{(44)}$$

3.2 Additional Heat Loss

Early results showed that the model consistently overpredicted the outlet temperature relative to the field data. There was a constant bias of approximately 6 °C. Several modes of heat loss were neglected in the development of the code. The sides of the absorber panel were considered adiabatic. Radiation between the collector and the roof was also ignored because of a lack of information about the roof's temperature. Setting this temperature to an arbitrary colder value than the collector underside yielded a negligible change in predicted working fluid temperature. Due to the way that the field site was instrumented, there was a large length of insulated pipe between the outlet of the solar collector, which is where the temperature was calculated by the code, and where the thermocouple data was recorded. A heat loss term was taken from the pipe as shown in Eq. 45, with a total resistance to heat flow described in Eq. 46. Here D_1 is the ¾" pipe that links the absorber panel to the heat exchanger, D_2 is D_1 plus an additional 1cm from the

insulation thickness, k_{ins} is the thermal conductivity of the rubber pipe insulation, L is the length of the pipe, and h_{ext} is an arbitrary 10 W/m^{2}K that accounts for the unknown forced and natural convection present on the outside of the pipe. Inclusion of this pipe heat loss greatly increased the accuracy of results.

$$T_{outlet} = T_{od} - (T_{od} - T_4)\exp\left(-\frac{1}{\dot{m}c_p R_{tot}}\right) \textbf{(45)}$$

$$R_{tot} = \frac{1}{\pi D_1 L h_{int}} + \frac{\ln(D_2/D_1)}{2\pi L k_{ins}} + \frac{1}{\pi D_2 L h_{ext}} \textbf{(46)}$$

3.3 Computational Methods

All programming was done in FORTRAN 95 and compiled with gfortran. The program first reads in the input data from the tab delimited text files. All temperatures are input as Fahrenheit and converted to Kelvin in the program.

The program then breaks the collector up into the specified number of substeps of equal size. These substep blocks are treated as individual heat transfer circuits with the specified input boundary conditions. There are two caveats however. First, the inlet working fluid temperature T_{in} of the first substep is set by the input file. When the heat transfer circuit converges and produces an outlet temperature T_4, that is then used as the working fluid temperature T_{in} for the next section, and so on along the length of pipe.

The other distinction to account for is that the convection coefficients are based on the temperature and aspect ratio of an entire surface. Since the fluid temperature changes a significant amount along the length of the piping, the temperatures at a particular layer throughout the various circuits will also be different. To address this, an average temperature was used for each layer in the calculation of convection heat transfer coefficients. Additionally convection values were calculated based on the actual size of the collector box, not the scaled area of the substep.

The initial values of the different average temperatures of the layers are guesses; for this reason, when the first substep's heat transfer circuit converges, it is slightly inaccurate

because its average temperatures were calculated using these bad guesses. After the first circuit is solved through, the average layer temperatures are recalculated using mostly guesses and the single converged value for the first circuit. After all circuits are converged, the average plate temperature is a much more accurate representation of the true value, and the code is repeated, this time beginning the first heat transfer circuit with the improved average temperatures.

Criteria for convergence of a heat transfer circuit were based on the change of each temperature's value from one iteration to the next. Due to the nonlinear effects of radiation heat transfer, the temperature difference between iterations was under-relaxed as shown in Eq. 47, where *i* refers to the temperature value and ω is the relaxation factor.

$$\Delta T = (T_{i,new} - T_{i,old})\omega \quad \textbf{(47)}$$

This ΔT was then added to the $T_{i,old}$ value to produce the updated value of temperature. When all six ΔT's were less than or equal a specified tolerance of 1E-5, the circuit was said to be converged. The converged T_4 value was set as T_{in} for the next substep's circuit and the process repeated. After the specified number of substeps had been solved, the process was repeated from the first substep, with T_{in} reset to the value of its boundary condition, until results of calculated capacity delivered to the water tank were determined to have converged. Convergence was defined as a percent change of capacity of less than 0.5%. Results show convergence in fewer than 5 of these iterations. A flow chart of the code's architecture is show below in Figure 17.

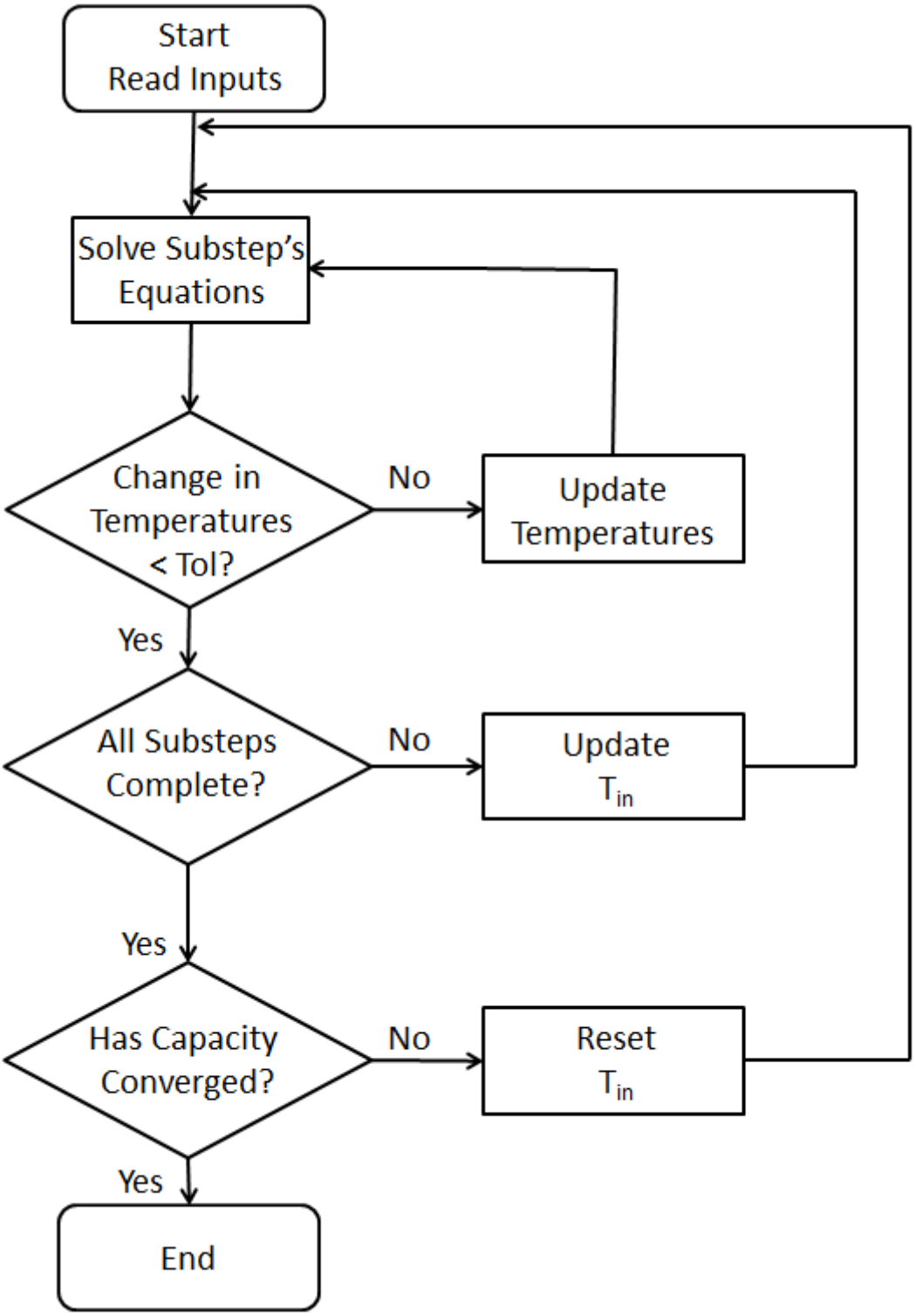

Figure 17. Program Flow Chart

At each substep, the temperature values and heat transfer coefficients are written to output files so the temperatures can be seen along the length of the pipe. Early results showed the temperatures of each layer increasing along the pipe length, as expected. The fluid temperature T_4 increases by the largest amount, with absorber temperature T_3 a close second, while the insulation underside T_5 and metal underside T_6 change the least. The magnitudes of these changes are dependent on the boundary conditions of a particular run.

The ΔT between T_2 and T_3 therefore changes along the length of the pipe, with a greater temperature potential at the end of the absorber panel. A changing temperature potential in natural convection could lead to the creation internal eddy currents. The model however assumes a single natural convection loop through Holland's correlation. Holland's correlation was used to determine if this change in temperature was significant for the cavity geometry used in validation. Using the same collector geometry, two pairs of temperatures that reflected those calculated in the cavity space produced natural convection coefficients with less than 7% difference. This was decided to be an insignificant change inside the cavity, and Holland's correlation was used.

Chapter 4: Results

4.1 Instrumentation and Data Collection

The house had a weather station mounted to its roof ridge to collect environmental data. A LiCor Li-200 was used to measure the normal solar irradiance in units of W/m^2. Next to this was a Vaisala HMP-50 which measured temperature in °F and relative humidity in %. This weather station was connected to Campbell Scientific Data Logger model CR23X. Data could be downloaded on demand via the home's internet connection. Interior to the house were four Onset HOBO temperature measurement devices, one connected under the insulation of each pipe on the indoor heat exchanger. The HOBOs stored their data internally and needed to be harvested and have their batteries replaced at regular intervals. Their lack of real-time information resulted in a loss of valuable winter data. The working fluid outlet temperature did not record from December 24, 2012 to March 6, 2013, making it impossible to validate the code against field data for that time period.

Aside from the physical instrumentation, the home utilized an eMonitor system. This service allows a home owner to monitor the energy usage of individual circuits throughout his home. The controller and pump were on a circuit together, and the instantaneous backup water heater was on a separate circuit, allowing the sources of water heating to be distinguished.

A Badger M 25 Flow Meter was converted to materials suitable for hot water applications. The standard dial display was removed and a magnetic switch was glued to the top of the meter so that its pulse output could be recorded with the data logger. This output was calibrated, and the meter was installed in the working fluid line set just past the heat exchanger. Its output was logged on the Campbell Scientific Data Logger. The data logger scanned at 15 second intervals and then averaged or totaled 60 measurements resulting in 15 minute data outputs.

In addition to the previously mentioned data loss from the HOBO, the solar water heating system went offline in mid-June. Because of the seamless transition to the instantaneous heating backup, this outage was not noticed for several weeks. A series of problems kept the system offline until late-October. The flow meter, while installed by a licensed plumber, leaked working fluid and later had to be removed. While operational, it did show that the system operates at a constant flow rate consistent with what the manufacturer advertises, thus serving its purpose. A leak in the water pipe leaving the water storage tank caused water damage to the working fluid pump. This unknowingly caused the pump to operate at too high of a current, causing a fuse in the controller pack to blow and disabling the controller. The controller was returned to the manufacturer and repaired, but since the root cause of the fault was unknown, the controller broke once again. After receiving technical support from the manufacturer, the cause was identified, and the controller and the pump were replaced. However, since the company is located in Canada, shipping and customs inspections further slowed down the repair process.

4.2 Validation

Fundamental assumptions required the input from field data to be taken near noon of each day. Only days with smooth irradiance data were used so that direct irradiance dominated diffuse. Five days were taken during Summer-like conditions and five days from Winter-like conditions. Due to lapses in both data collection and system operation, days specifically during these seasons are unavailable. However days from late May and late November/early December are used. Figure 18 shows the code's predicted working fluid outlet temperature, corrected for heat loss in the piping, as a function of actual measured working fluid temperature. The solid line denotes a 1:1 relationship; the closer the data points are to this line, the more accurate the results.

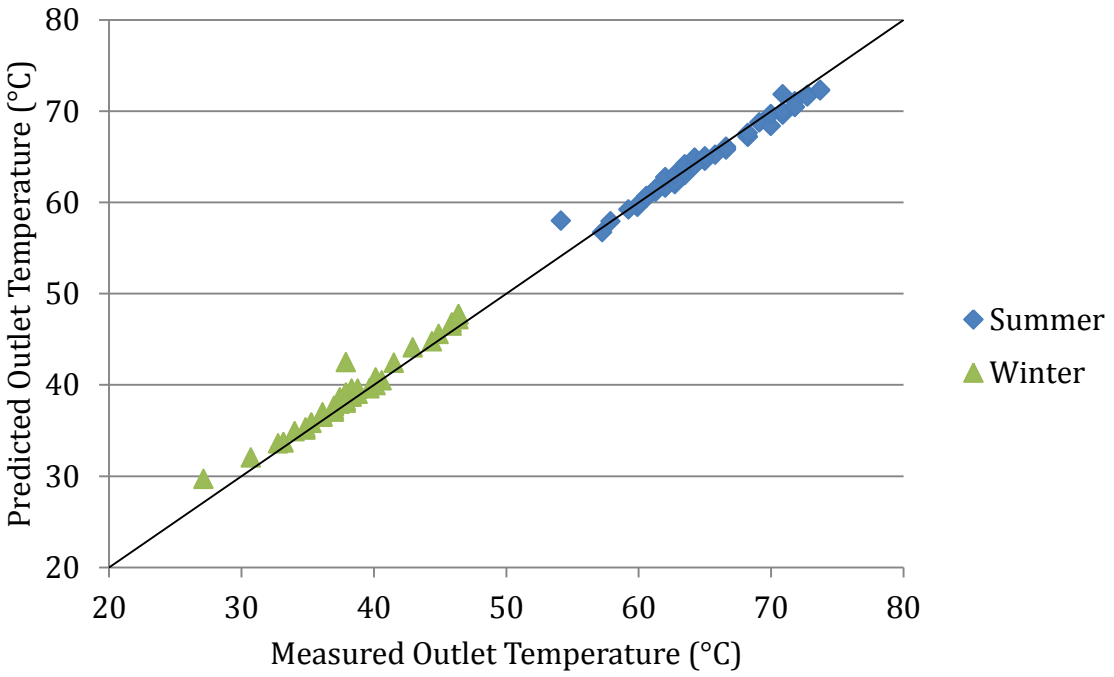

Figure 18. Outlet Temperature Validation

The plot shows an excellent amount of accuracy to the field data. There are several outliers which can be explained. These values occurred when there was a sudden drop in collector inlet temperature, which would correspond to a water draw from the house, resulting in cold water being added to the water loop. Removing these three instances yields a maximum error of 1.6 °C, and the average absolute value of error is 0.6 °C. To normalize the data point of each case, the percent error was calculated as the absolute difference between measured and predicted temperatures divided by the measured temperature difference. This produced an average percent error of 7.45%. In the Summer-like data, the code tends to underpredict the fluid temperature; in Winter-like data it tends to overpredict.

The absorber panel certification efficiency was also provided as a 2nd order curve fit in the manufacturer's rating document. This was compared against the measured absorber panel efficiency, calculated using Eq. 48, where piping heat loss is not considered.

$$\eta_{meas} = \frac{\dot{m}c_p(T_4 - T_{in})}{I * A_{panel}} \quad \textbf{(48)}$$

Figure 19 shows calculated efficiency versus manufacturer efficiency. The results during the Summer-like weather are remarkably accurate, with the largest error being only .84%. In the Winter-like months, the model consistently and significantly overpredicts the collector's efficiency relative to the manufacturer's values. It has on average an error of 3.9%. The larger error is probably due to assuming sky temperature equal to outdoor temperature which is less accurate for winter months.

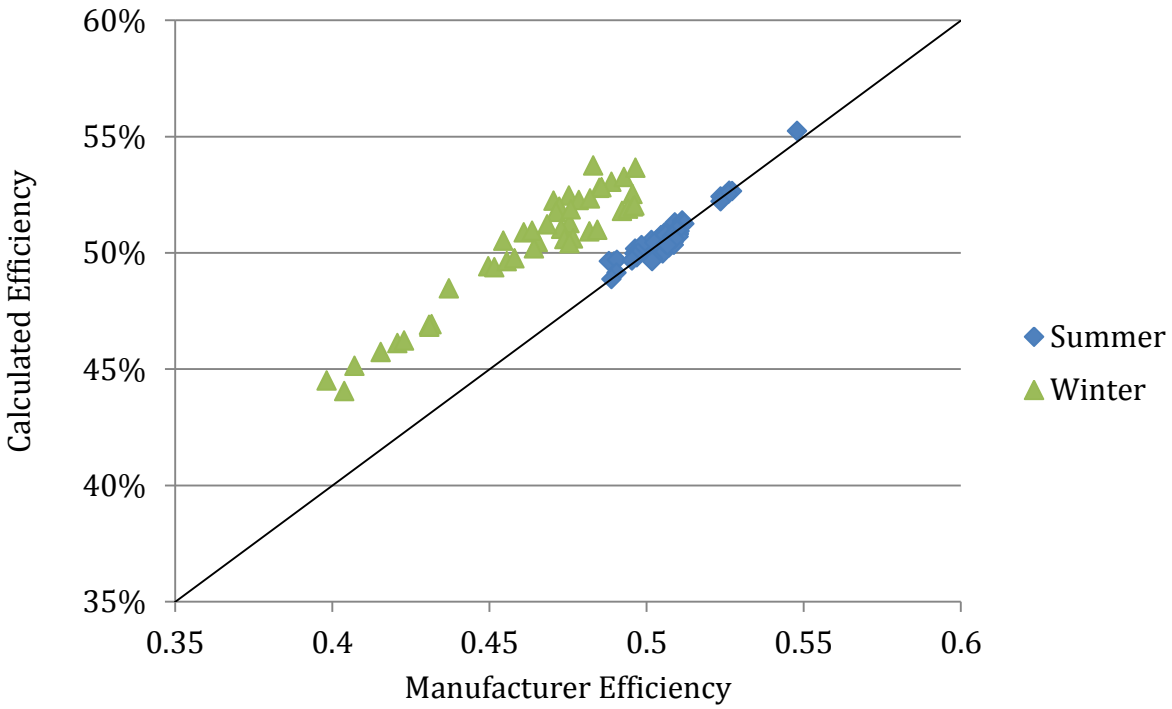

Figure 19. Efficiency Validation

4.3 Sensitivity Analysis

Dividing the plate into smaller one-dimensional sections allows for many of the assumptions made in the code. Therefore the number of substeps should be chosen in such a way that they converge on an output. For this study, the most important factor is the working fluid outlet temperature, which is directly relatable to capacity delivered to the

water tank. For a day on which the code matched the data especially well, the code was run with different inputs for the substeps it should take. Figure 20 shows the code's temperature output as a function of substeps taken. A significant change in predicted temperature is observed when changing the substeps from 1 to 10. Increasing the substeps from 40 to 50 resulted in a change of reported working fluid outlet temperatures of less than 0.2%. 50 substeps were taken as the input for all further benchmarking.

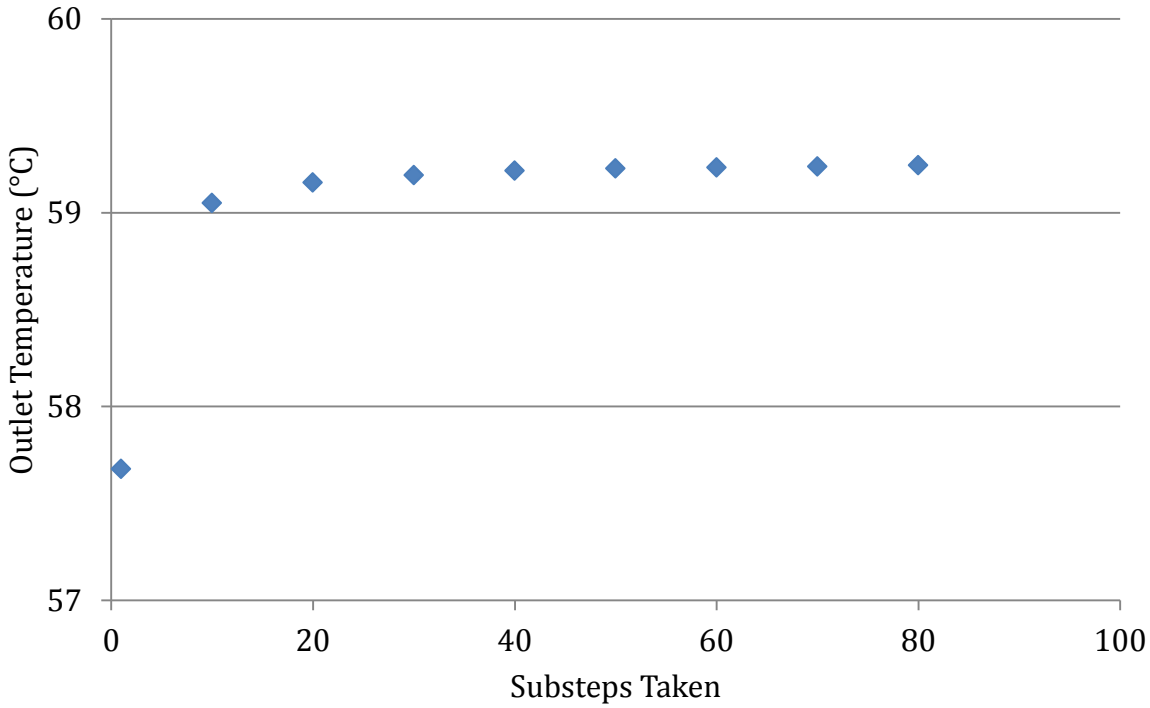

Figure 20. Substep Sensitivity

The largest source of uncertainty in boundary conditions came from the wind speed. This data was unavailable at the field sites and was instead based on the recorded data from the website Weather Underground[24]. Data was not recorded in Norris; the closest location available was Oak Ridge, TN. For the three hour time period during which results were obtained, an average wind speed was taken based on that record. A sensitivity analysis was performed on a day with especially accurate results to see what affect wind speed had on the final results, and is presented in Figure 21. The wind speed on this particular day was assumed to be 3.35 m/s. A lower input velocity had a small effect,

increasing outlet temperature by less than 0.5%. At 3.34 m/s, turbulence appears on the collector. As velocity increases, the boundary layer above the collector becomes more predominately turbulent, causing greater heat loss through the top surface. This is evident from the figure. Still, even at 13 m/s, the calculated outlet temperature changed by less than 3 °C. This speed corresponds to 29 mph, which would be wind gusts and not have a sustained impact on the solar collector. This shows that low wind speeds have a minor effect on predicted values, but beyond 3.34 m/s, they begin to have a more pronounced effect.

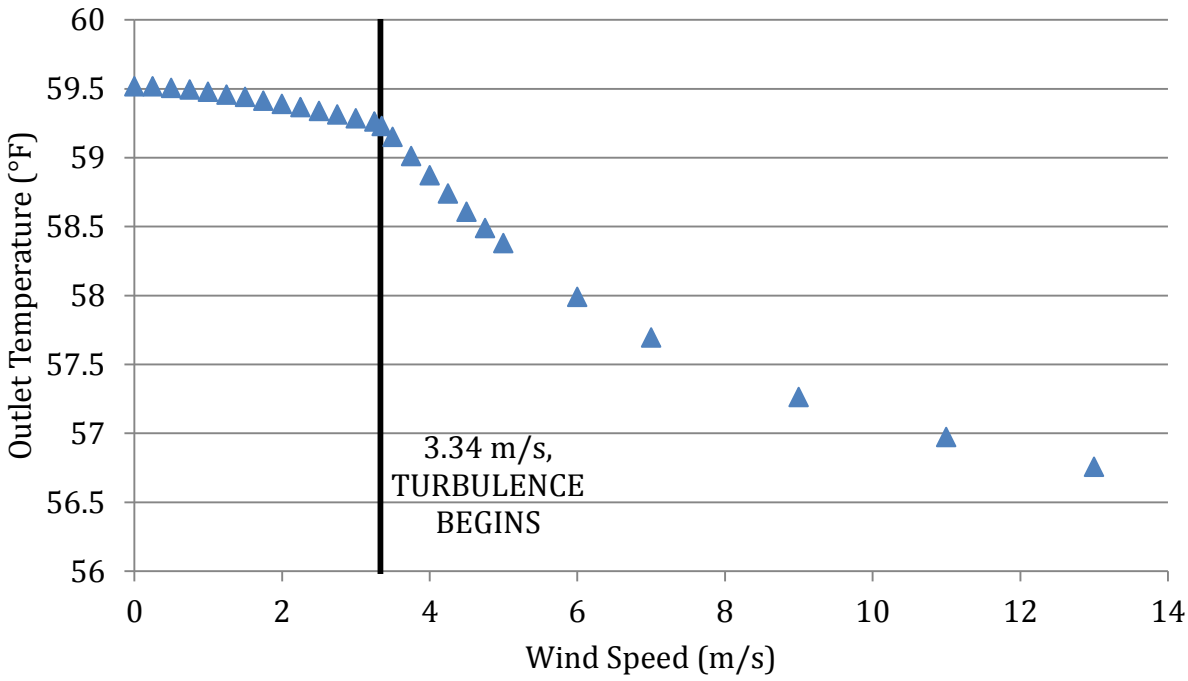

Figure 21. Wind Speed Sensitivity

The other significant unknown was the reflectance of the top pane of glass. While transmittance was specified as 0.91 in manufacturer literature, no information of reflectance was publically available. In the validation, the reflectance of both sides was assumed to be that of clear glass, 0.0748. Since the sum of Tr, Rf, and Ab cannot exceed 1, Rf was varied from 0.00 to 0.09 for the same sample day. The results of those trials are shown below in Figure 22. Again there is not a large change in temperature due to this unknown

parameter. Across the entire range of possible values for Rf, the outlet temperature changes by only 0.8 °C. This shows the model is not greatly affected by this property's uncertainty.

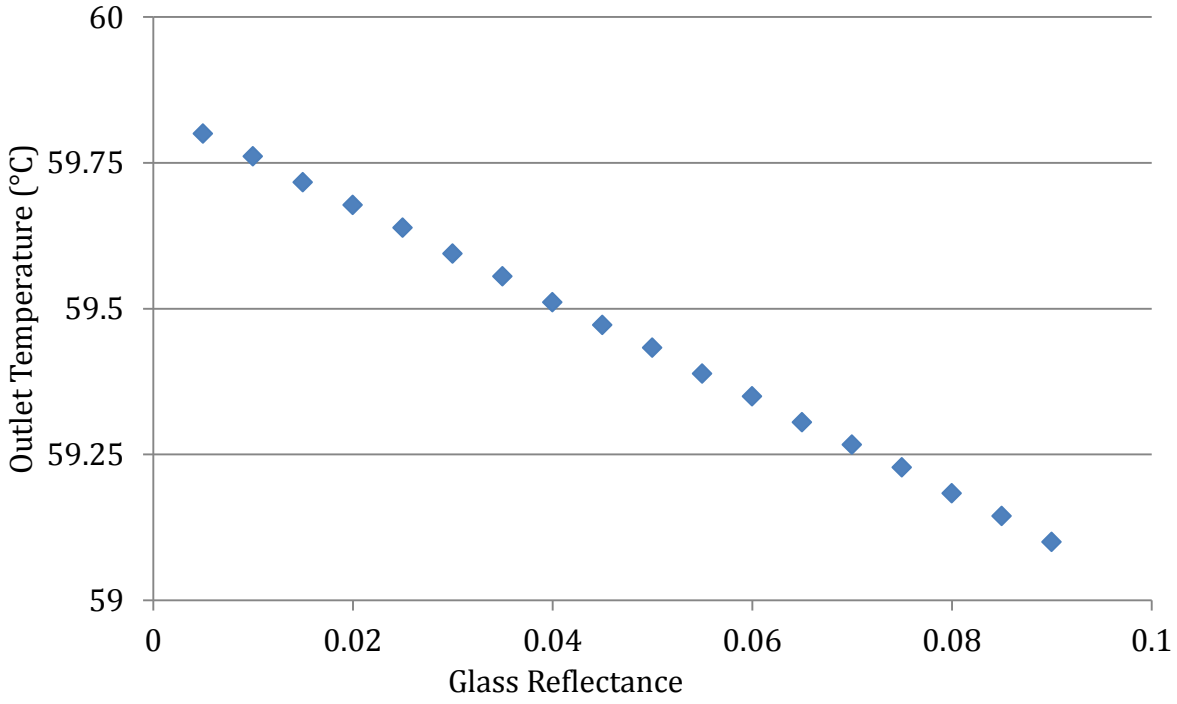

Figure 22. Glass Reflectance Sensitivity

4.4 Laboratory Benchmarking

In addition to field data validation, a rating report was made available by EnerWorks. The contents of this report are confidential, but it provided the boundary conditions of the solar collector during laboratory evaluation by Bodycoate Materials Testing. Among these tests were two ratings conducted with different irradiance values at a normal angle to the collector's surface. This was ideal for benchmarking the model because the model does not take into account the Sun's angle with the top surface. Several inputs to the code were modified to better reflect the rating setup. The underside convection coefficient was artificially reduced by a factor of ten and the tilt angle was changed to 0°.

Also, the rating method measured fluid temperature as it left the collector, so the pipe heat loss term was disabled for this comparison. Table 2 summarizes the two conditions the model was compared against. When the rating conditions were run through the model, it predicted the outlet fluid temperature with an error of 0.54 °C for the lower of the irradiances, and an error of 0.10 °C for the higher of the irradiances. In both cases, the model underpredicted the laboratory data.

Table 2. Model Comparison to Laboratory Data

Parameter	Value
Test 1	
Normal Irradiance	808 W/m^2
T_{od}	20.1 °C
T_{in}	20.0 °C
Wind Speed	3.5 m/s
$\dot{m}$	0.0543 kg/s
Laboratory T_{out}	28.5 °C
Predicted T_{out}	28.4 °C
Error	0.1 °C
Percent Error	6.34%
Test 2	
Normal Irradiance	787 W/m^2
T_{od}	20.1 °C
T_{in}	20.0 °C
Wind Speed	3.5 m/s
$\dot{m}$	0.056 kg/s
Laboratory T_{out}	28.5 °C
Predicted T_{out}	28.0 °C
Error	0.5 °C
Percent Error	1.18%

4.5 Sample Case

The manufacturer asked that the details of their collector design not be revealed. The dimensions and properties that were used to produce this chapter's results have therefore not been discussed in this work. However, for the purposes of future comparison, a sample case is now presented with all the inputs and results listed in Table 3. The additional heat loss from the piping is not considered.

Table 3. Input Values for Sample Case

Pipe Length	15 m
Substeps	50
Wind Speed	3.0 m/s
Collector Tilt	2°
Collector Height	1 m
Collector Width	2 m
Internal Air Gap Height	0.07 m
Glass Thickness	0.003 m
Glass Thermal Conductivity	1 W/mK
Pipe Diameter	0.01m
Fluid Mixture	50/50 Propylene Glycol/Water
Volumetric Flow Rate	0.25 GPM
Insulation Thickness	0.035 m
Insulation Thermal Conductivity	0.05 W/mK
Metal Thickness	0.0005 m
Metal Thermal Conductivity	237 W/mK
Emissivity of Glass	0.84
Emissivity of Absorber	0.9
Transmittance of Glass	0.91
Transmittance of Absorber	0
Reflectance of Glass	0.07
Reflectance of Absorber	0.1
Irradiance	900 W/m^2
T_{od}	25 °C
T_{in}	50 °C
Calculated T_4	66.6 °C

Chapter 5: Conclusions

The model developed in this work proved to be accurate, albeit with certain limitations. Its function is to calculate the temperature of working fluid after it has passed through a serpentine flow flat plate solar absorber panel close to solar noon. Complete information was not available on the geometry and materials of the absorber panel. Reasonable assumptions were made to fill in the unknown aspects. Additionally, the wind speed boundary condition was not well known. Sensitivity analysis showed that these unknowns were not a major driver in the outlet temperature, except for large wind speeds. More accurate wind data should lead to more accurate results.

When heat loss from the collector to the instrumentation was accounted for, the code matched well with the available field data. Temperatures were predicted with an average error of 0.62 °C to field site data. By using boundary conditions at the appropriate times of day, values for working fluid outlet temperature were sufficiently close to measured field data considering the level of uncertainties. The model was also benchmarked against laboratory tests with errors of 0.54 °C and 0.10 °C. Additional assumptions made in the calculation of piping heat loss and transient boundary conditions could explain the larger error seen from field site validation.

In Summer-like months, efficiencies were predicted very accurately to the manufacturer's reported equation. In Winter-like months, the code consistently overpredicted efficiency. Both periods had an efficiency of approximately 50%. Laboratory benchmarking also closely predicted the reported efficiency of approximately 74%. This field study demonstrates the practicality of solar water heating systems. Commercial photovoltaic panels can vary in efficiency from 10% to 40%[25]. That fact demonstrates that a dedicated solar water heater will supplement more power to a home than a system that produces electricity for resistance heating for the same sized panel.

Using the inlet and outlet temperature, the supplemental heating capacity delivered to the water can be determined. Data for Summer-like weather showed 800 W-1000 W and data for Winter-like weather showed 400 W- 500 W being delivered to the water tank.

Table 4 summarizes the average capacities for measured and predicted cases in both seasons investigated.

Table 4. Average Seasonal Capacities

Type	Average Capacity (W)
Measured Summer-like	927
Predicted Summer-like	905
Measured Winter-like	420
Predicted Winter-like	474

This shows that in warm and cold seasons, over 900 W and 400 W of water heating were provided by the solar collector. Due to data collection issues, the peak Summer months of June and July are not available, but the increased irradiance and lower potential between T_i and T_{od} during these times would lead to even more power availability. The eMonitor system recorded the power consumption of the working fluid pump as approximately 50 W, yielding a significant amount more power delivered than used.

The model in this work was meant to be the first phase of a much more detailed work. It demonstrated the ability to discretize successfully a serpentine style flat plate collector in a 1 dimensional sense. It additionally incorporated the effects of environmental convection on the collector surface. The net radiation technique allowed for the incorporation of shortwave radiation at an averaged wavelength.

Calculations showed that for the field site approximately 42% of the power provided by the Sun was lost to the environment through the top of the collector. To improve the efficiency of the absorber panels, additional glass panes could be added to reduce this heat loss.

Future development of this model would allow for a more accurate representation of environmental conditions that affect radiometric calculations for glazings containing multiple panes of glass. By incorporating the irradiance intensity across the solar spectrum, glazing and film properties can be included to model materials that are selective of solar wavelength. Using the net radiation technique already described in this work, additional

glass layers may be added to predict the effects of different glazing subsystems in cold climate application.

List of References

1. Norton, B., *The Centenary of Solar Collectors for Heating Water*, in *World Renewable Energy Congress 2011*. 2011: Linköping, Sweden. p. 1.
2. Grondzik, W.T., *Mechanical and electrical equipment for buildings*. 11th ed. 2010, Hoboken, N.J.: Wiley. pp 153,946-957.
3. Energy Information Administration. *Residential Enercy Consumption Survey*. 2009 [cited 2013 July 31]; Available from: http://www.eia.gov/consumption/residential/.
4. KSENYA. *Flat Plate Solar Collectors*. 2011 [cited 2013; Available from: http://solartribune.com/flat-plate-solar-system/.
5. Hudon, K., Merrigan, T., Burch, J., and Maguire, J. *Low-Cost Solar Water Heating Research and Development Roadmap*. 2012, National Renewable Energy Laboratory: Golden, Colorado.
6. SRCC, *Test Methods and Minimum Standards for Certifying Solar Collectors*.
7. ASHRAE, *Methods of Testing to Determine the Thermal Performance of Solar Collectors*. 2010: Atlanta, GA.
8. T.P., Chang. *The Sun's apparent position and the optimal tilt angle of a solar collector in the northern hemisphere.* Solar Energy, 2009. **83**(8): p. 1274-1284.
9. Kennedy, C., *Progress to Develop an Advanced Solar-Selective Coating*. 2008, SolarPACES: Las Vegas, Nevada. p. 8.
10. Gueymard, C.A. and W.C. duPont, *Spectral effects on the transmittance, solar heat gain, and performance rating of glazing systems.* Solar Energy, 2009. **83**(6): p. 940-953.
11. Duffie, J.A. and W.A. Beckman, *Solar Engineering of Thermal Processes*. 3rd ed. 2006, Hoboken, N.J.: John Wiley. 908 p.
12. Villar, N.M., Lopez, J. M., Munoz, F.D., Garcia, E.R., Adnres, A.C. *Numerical 3-D heat flux simulations on flat plate solar collectors.* Solar Energy, 2009. **83**(7): p. 1086-1092.
13. Wills, A.D., *Design and co-simulation of a seasonal solar thermal system for a Canadian single-family detached house*, in *Department of Mechanical and Aerospace Engineering*. 2013, University of Windsor. p. 221.

14. Lund, K.O.F., *General thermal analysis of serpentine-flow flat-plate solar collector absorbers.* Solar Energy, 1989. **42**(2): p. 133-142.
15. Stuth, T., Mortimer, S., Friedman, V., Buchanan, J. *A New Norris House: Making Criteria for Sustainable Landscapes Visible*. 2013, ARCC: Spring Research Conference.
16. Batey, R., *New Norris House*. 2013.
17. Mortimer, S., *Lessons Learned: A New Norris House*. 2013. p. 7.
18. Iternational Orginzation of Standardization, *Thermal Performance of Windows, Doors and Shading Devices-Detailed Calculations*. 2002.
19. Incropera, F.P., DeWitt, D.P., Bergman, T.L., Lavine, A.S., *Fundamentals of Heat and Mass Transfer*. 6th ed. 2007, Hoboken, NJ: John Wiley.
20. Rohsenow, W.M., Hartnett, J.P.,and Ganić, E.N. *Handbook of Heat Rransfer Fundamentals*. 2nd ed. 1985, New York: McGraw-Hill. pp. 7.20-7.32.
21. Çengel, Y.A., *Heat and Mass Transfer : A Practical Approach*. 3rd ed. 2007, Boston: McGraw-Hill. 901 p.
22. Azevedo, L. F. A, Sparrow, E.M., *Natural Convection in Open-Ended Inclined Channels.* Journal of Heat Transfer, 1985. **107**(4): p. 9.
23. Siegel, R., *Net radiation method for transmission through partially transparent plates.* Solar Energy, 1973. **15**(3): p. 273-276.
24. *Weather History and Data Archive*. 2013 [cited 2013 Septermber]; Available from: http://www.wunderground.com/history/.
25. *NREL: National Center for Photovolatics*. 2013 May 14, 2013 [cited 2013; Available from: http://www.nrel.gov/ncpv/.

Vita

Zeke Stannard earned his Bachelor of Science degree in Mechanical Engineering from the University of Tennessee in December of 2011 with Summa Cum Laude honors. During his time as an undergraduate he held two separate internship appointments at Oak Ridge National Lab, where he aided in the testing of new Hydrogen production techniques through electrolysis and evaluated the performance of the ZEBRAlliance test homes. He continued his education at the University of Tennessee for his Master of Science degree in Mechanical Engineering. During his time as a Master's student he worked at the Electric Power Research Institute in the Power Delivery and Utilization sector.